Damage Initiation Prediction in Textile Composites for Deployable Space Structures based on Tape Springs

By

Francisco Javier Hernández Calvo

in partial fulfilment of the requirements for the degree of

Master of Science
in Aerospace Engineering

at the Delft University of Technology

November 10, 2017

Supervisors: Sonell Shroff, Julien Ducarne

TU Delft

Abstract

Deployable structures using tape-springs are a promising option to minimize the volume occupied by satellites at launch and reduce launching costs. The attractive characteristics of tape-springs made of ultra-thin woven composites are their high specific stiffness and bi-stable behavior. However, the most important shortcoming is the complexity of their mechanical analysis. Textile composites are formed by the weaving of bundles of fibers creating a very complex microstructure, and tape-springs present a highly nonlinear mechanical behavior subjected to multi-axial loadings. Therefore, conventional mechanical models developed for unidirectional lamina no longer apply since they do not take into account stress gradient effects through the representative volume element (RVE). In this work, a multi-scale approach is validated to predict the failure initiation of tape-springs. Micromechanical models are used to predict analytically the stiffness properties of the fiber bundles, while FE-mesoscale models describe the woven structure and provides stiffness and strength properties for computations on macroscale. A case study of hybrid laminates composed of woven and unidirectional layers is analyzed for its application on tape-springs. Manufacturing defects related to ply waviness of the UD layer have been detected and taken into account to estimate the reduction of the overall stiffness properties. Finally, a dedicated failure criteria based on the force and moment resultants have been used to predict failure initiation of the tape-springs under multi-axial loading conditions. A good correlation was found between the finite element analysis and experimental observations.

Contents

List of Figures

List of Tables

Chapter 1 Introduction

The concept of deployable structures allows large satellites to be packed compactly during transportation which can be expanded back for operation. This may enable space structures to have larger dimensions than the available payload volume of a launcher. Tape-springs are thin-walled self-deployable strips that can be highly elastically deformed. Deployable structures made of composite tape-springs are a promising option to pack space structures because of their low coefficient of thermal expansion and low mass to deployed stiffness ratio [1]. The use of woven composites is presented as one of the best options to obtain tape-springs with tight coiled stable state, which allows very compact and lightweight designs.

The space industry design standards require a structure to avoid any type of failure, thus an accurate prediction of damage onset is essential for the safest and yet, optimized design [2]. Although numerous failure theories to predict damage behaviour have been developed for unidirectional composite plies, this task becomes particularly complicated in woven laminates subjected to complex loading conditions. For example, stress gradients can be seen in an individual fibre tow due to the complexity of the weave geometry. Dedicated failure theories are still under development.

1.1 Aim

The goal of this thesis is to validate a model to predict the failure initiation of tape-springs made of woven composites that are subjected to multiaxial loadings by using a multi-scale approach that considers stress gradient effects through the representative volume element of the woven composite.

Based on the thesis objective, the following research questions are proposed:

1. How accurately is it possible to predict the stiffness and failure initiation of woven composites by using a multi-scale approach that idealizes the RVE of the actual woven composite by considering elliptical/lenticular section yarns and homogenized elastic properties?
    a. Is it acceptable to assume a simplified RVE when compared to experimental data?
    b. Does the effect of these assumptions vary between plain and twill weave patterns?
2. What is the best weaving pattern to be used in composite tape-springs for deployable space structures?
    a. How does the weaving pattern affect the overall stiffness of tape-springs?
    b. Is there a significant change in the failure initiation load due to the weaving pattern?

1.2 Context

This thesis has been carried out at Thales Alenia Space (TAS) in the in the Research and Technology (RT) department. The project is part of an ambitious program that seeks to develop new deployable

satellite systems to face new market trends. Specifically, the thesis is focused on the damage initiation prediction in textile composites for deployable structures based on tape-springs.

On the one hand, most of the work previously done by the department has been focused on thermo-mechanical properties characterization of woven fabrics by using conventional mechanical models such as the Classical Laminate Theory. These models assume that either the stress or the strain state is uniform across a representative volume element (RVE) of the textile composite, which is the smallest part to represent the homogenized properties of the macroscopic material. Although this assumption may be valid to predict in-plane thermo-elastic properties, there are significant deviations in the flexural properties, especially for thin woven laminates [3]. This thesis hypothesizes a dedicated micromechanical approach that includes non-uniform stress considerations in order to determine the multiaxial stiffness of woven composites.

On the other hand, there has been little or no work on the failure initiation prediction of hybrid textile composites subjected to multiaxial loadings. Textile composites are formed by the weaving of bundles of fibers creating a very complex microstructure. Therefore, conventional failure theories developed for unidirectional lamina no longer apply. This thesis validates a dedicated failure initiation theory that accounts for the interactions between yarns in the mesoscale level when complex multi-axial loads are applied in the macroscale level.

1.3 Outline

This dissertation is organized in six chapters. After the present introduction, Chapter 2 presents a review of the mechanical behaviour of deployable structures based on tape-springs. The characteristics of woven composites are introduced, and the existing modelling techniques to analyse them are compared. Chapter 3 describes the FE unit cell approach and presents the micromechanical model used to homogenize the mechanical properties of woven composites. The failure analysis procedure is validated using three different weave laminates under different loading conditions. Chapter 4 extends the application of the unit cell approach to hybrid composites based on woven and unidirectional layers, whose peculiarities are analysed by making use of micrographs. The mechanical properties of the laminates are estimated and the results are used in Chapter 5 to predict the macroscopic failure behaviour of tape-springs subjected to multi-axial loading. Finally, Chapter 6 presents the overall conclusions and suggest a set of recommendations for future research.

Chapter 2 Background and Literature Study

2.1 Deployable Space Structures

There is great interest in developing innovative compact structures that require no external source of energy when deployed in orbit. The goal is to reduce launching costs by making efficient use of the available payload volume, i.e. minimize the volume occupied by the satellite at launch. Since the mass is also an important limiting factor, deployable elastic structures are a promising alternative to heavier structures with articulated joints. Thales Alenia Space is working on new satellite concepts based on tape-springs.

Tape-springs have been typically made from well-known materials such as steel or copper-beryllium alloys. However, materials with near-zero coefficient of thermal expansion (CTE) and high specific stiffness are required in support structures of high technology satellites. Fiber-reinforced composite materials with in-plane CTE that is near zero can be achieved by varying the orientation of plies having positive and negative CTEs [4].

Another essential requirement is to ensure that no damage occurs during the operational life of the satellite. Damage tolerance philosophy is adopted in the aeronautical industry with regular aircraft maintenance. However, this philosophy is no longer valid in the space industry, where satellites cannot be repaired after launch. Therefore, the strength of the composite tape-springs must be high enough to avoid failure initiation.

During launch, the spacecraft experiences the most critical loading conditions. The satellite structure must prevent launch vibrations from harming the payload instruments [5]. The structure will be in the stowed position, with the tape springs loaded in tension to handle the dynamic launch loads. However, due to the tape spring mechanical behavior there is a moment required to flatten the tape-springs as shown in Figure 1. Therefore, the tension force in the stowed position leads to a complex loading state that will define the strength requirements of the tape-springs.

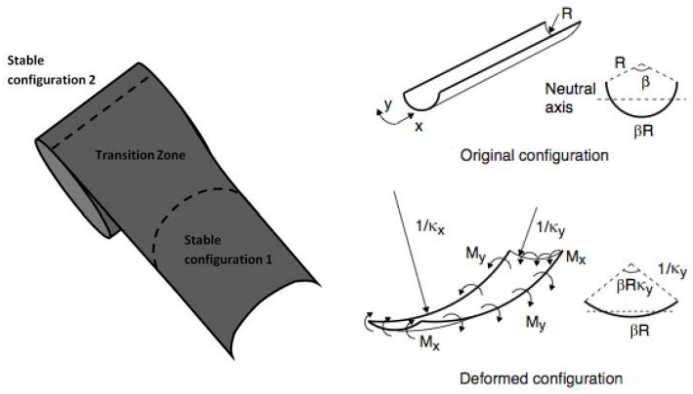

Figure 1. Tape-spring configurations [6, 7]

2.2 Bi-stable Tape Springs

Tape-springs are thin-walled strips, with a constant curved cross-section in its free state as shown in Figure 1 at top-right. They can be compared to a straight beam that can be folded elastically and capable of deploying themselves by releasing the stored strain energy [8]. This allows the use of lightweight guides to control the structure deployment without the need of actuators. Tape-springs may have two stable states if made from fiber-reinforced composites: an extended state where there is no energy stored, and a tight coiled state. Both correspond to equilibrium configurations, i.e. the strain energy has zero slope for small variations in the principal curvature κ_x and the angle β sub-tended by the cross-section (see Figure 1). However, these configurations will be stable only if the energy is at a local minimum. On the one hand, the extended state is clearly stable since there is no strain energy stored. On the other hand, the coiled state satisfies the stable equilibrium conditions if there is no coupling between bending and twisting ($D_{16} = D_{26} = 0$), and if the following expression is positive [9].

$$4\frac{D_{66}}{D_{11}} + 2\frac{D_{12}}{D_{11}} - 2\frac{D_{22}}{D_{11}D_{12}} > 0 \tag{1}$$

where D_{ij} are coefficients of the [ABD] matrix, which relates forces and moments to strains and curvatures for any laminate as follows:

$$\begin{Bmatrix} N_x \\ N_y \\ N_{xy} \\ M_x \\ M_y \\ M_{xy} \end{Bmatrix} = \begin{bmatrix} A_{11} & A_{12} & A_{16} & B_{11} & B_{12} & B_{16} \\ A_{12} & A_{22} & A_{26} & B_{12} & B_{22} & B_{26} \\ A_{16} & A_{26} & A_{66} & B_{16} & B_{26} & B_{66} \\ B_{11} & B_{12} & B_{16} & D_{11} & D_{12} & D_{16} \\ B_{12} & B_{22} & B_{26} & D_{12} & D_{22} & D_{26} \\ B_{16} & B_{26} & B_{66} & D_{16} & D_{26} & D_{66} \end{bmatrix} = \begin{Bmatrix} \varepsilon_x \\ \varepsilon_y \\ \gamma_{xy} \\ \kappa_x \\ \kappa_y \\ \kappa_{xy} \end{Bmatrix} \tag{2}$$

The advantage of the bi-stable tape springs is that they avoid the need of a mechanism to retain the coiled configuration, which results in a very compact and lightweight design.

The two bi-stability conditions mentioned above can be achieved by anti-symmetric layups using unidirectional plies. However, such laminates may have significant in-plane/out-of-plane coupling since the [B] matrix terms are not zero. This generally leads to out-of-plane distortions during manufacturing and operation in space environment due to thermal loads. The use of woven fabrics is a

better option because laminates with zero [B] matrix can be obtained, as it is further explained in Section 2.3. Furthermore, textile composites present higher interlaminar strength in comparison to composites made from UD lamina. Fiber undulation in the thickness direction contributes to enhanced out-of-plane mechanical properties and resistance against delamination [10, 11].

2.3 Textile Composite Materials

Textile composites can be classified as woven, braided and knitted fabrics according to the machines and processes used to arrange their reinforcing elements [12]. From this classification, Thales Alenia Space is particularly interested in woven composites because of their versatility and desired mechanical properties in bi-stable tape springs. Textile composites materials are made using continuous bundles of fibers, called yarns or tows, and the matrix that binds them together. Woven fabrics are formed by interlacing two sets of tows, referred to as warp and weft yarns. Some examples of interlacing patterns are shown in Figure 2 below.

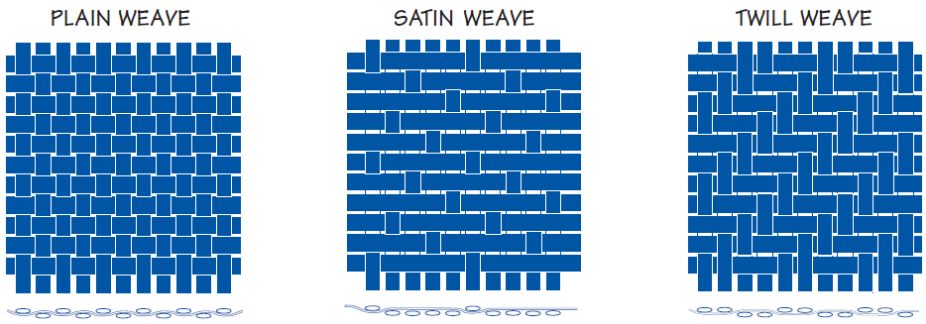

Figure 2. Weave style of plain, satin and twill fabrics [13]

The weave styles shown in Figure 2 above are periodic, thus only a representative volume element (RVE) is needed to represent the homogenized properties of the macroscopic material. Symmetric woven styles are of particular interest because laminates with no bending/torsion coupling and no in-plane/out-of-plane coupling can be obtained. This can be explained by looking at the plain weave style shown in Figure 2. First, it could be argued that the stacking sequence matrix/fill/warp/matrix is asymmetric, and thus extension/bending coupling will exist. However, the exactly opposite undulation of two adjacent fill/warp yarns leads to opposite signs for the in-plane/out-of-plane local coupling coefficients that will cancel each other [14]. Therefore, the overall extension/bending effect is restrained, which is necessary for the correct mechanical behaviour of tape-springs as it is pointed out in Section 2.2.

Within the group of symmetric weaving patterns, the plain weave stands out due to the excellent fabric stability as well as the simplicity and smaller size of the repetitive unit cell. The disadvantage of this pattern is that it presents a high degree of waviness or yarn crimp that negatively affects the in-plane stiffness properties [15]. However, Thales Alenia Space reduces this effect by using low tex (fibers per yarn) bundles.

The complex structure of woven composites makes the experimental evaluation of the material properties very difficult. Tests for obtaining the material parameters in the thickness directions would be required, which are not easy to perform. Furthermore, this approach is not feasible at the

early stages of design when many iterations are required. Virtual tests using a multi-scale analysis approach are an attractive alternative to experiments as demonstrated by many authors.

The multiscale analysis consists of three levels, micro, meso, and macroscale. Stiffness properties of fiber bundles can be determined with micromechanical models. The mesoscale describes the woven structure and provides stiffness and strength properties for computations on macroscale [16].

2.3.1 Micro-mechanical modeling

The fiber and matrix are discretized in the microscale, where the transversely isotropic material parameters of the yarns are obtained. The homogenized elastic properties could be well predicted using simple analytical models such as the Rule of Mixtures and Chamis equations [17]. Although Chamis model yields very good results and is widely used to calculate the longitudinal extensional modulus E_1, see Equation (3), and the Poisson's ratios, see Equation (4), Younes et al. [18] showed that the Halpin-Tsai model [19] enhances the prediction of the transverse extensional modulus E_2, see Equation (6), and shear modulus $G_{12} = G_{13}$, see Equation (5). The transverse shear modulus G_{23} represents the main challenge since the results do not agree so well with experimental data. For this, Quek et al. [20] recommend using the expression shown in Equation (8), developed by Christensen and Waals [21] in order to get accurate results. Therefore, taking into account that FE methods do not prove to be more accurate [18], the independent engineering constants can be calculated as follows.

$$E_1 = E_{1f}V_f + E_m(1 - V_f) \tag{3}$$

$$\upsilon_{12} = \upsilon_{13} = \upsilon_{12f}V_f + \upsilon_m(1 - V_f) \tag{4}$$

$$G_{12} = G_{13} = G_m \frac{(G_{12f} + G_m) + V_f(G_{12f} - G_m)}{(G_{12f} + G_m) - V_f(G_{12f} - G_m)} \tag{5}$$

$$E_2 = E_3 = E_m \frac{1 + \chi\eta V_f}{1 - \eta V_f} \tag{6}$$

where χ is a parameter that depends on the fiber geometry and loading conditions (Daniel and Ishai, 2006), and η is calculated as:

$$\eta = \frac{E_{2f} - E_m}{E_{2f} - \chi E_m} \tag{7}$$

The transverse shear modulus G_{23} is given by solving the following equation:

$$\left(\frac{G_{23}}{G_m}\right)^2 A + \left(\frac{G_{23}}{G_m}\right) B + C = 0 \tag{8}$$

where

$$A = 3V_f(1-V_f)^2\left(\frac{G_{12f}}{G_m}-1\right)\left(\frac{G_{12f}}{G_m}+\zeta_f\right)+\left[\left(\frac{G_{12f}}{G_m}\right)\zeta_m+\zeta_m\zeta_f-\left(\left(\frac{G_{12f}}{G_m}\right)\zeta_m-\zeta_f\right)(V_f)^3\right] \times\left[\zeta_m V_f\left(\frac{G_{12f}}{G_m}-1\right)-\left(\left(\frac{G_{12f}}{G_m}\right)\zeta_m+1\right)\right] \tag{9}$$

$$B = -6V_f(1-V_f)^2\left(\frac{G_{12f}}{G_m}-1\right)\left(\frac{G_{12f}}{G_m}+\zeta_f\right)+\left[\left(\frac{G_{12f}}{G_m}\right)\zeta_m+\left(\frac{G_{12f}}{G_m}-1\right)V_f+1\right] \times\left[(\zeta_m-1)\left(\frac{G_{12f}}{G_m}+\zeta_f\right)-2(V_f)^3\left(\left(\frac{G_{12f}}{G_m}\right)\zeta_m-\zeta_f\right)\right] + (\zeta_m+1)V_f\left(\frac{G_{12f}}{G_m}-1\right)\times\left[\frac{G_{12f}}{G_m}+\zeta_f+\left(\left(\frac{G_{12f}}{G_m}\right)\zeta_m-\zeta_f\right)(V_f)^3\right] \tag{10}$$

$$C = 3V_f(1-V_f)^2\left(\frac{G_{12f}}{G_m}-1\right)\left(\frac{G_{12f}}{G_m}+\zeta_f\right)+\left[\left(\frac{G_{12f}}{G_m}\right)\zeta_m+\left(\frac{G_{12f}}{G_m}-1\right)V_f+1\right] \times\left[\frac{G_{12f}}{G_m}+\zeta_f+\left(\left(\frac{G_{12f}}{G_m}\right)\zeta_m-\zeta_f\right)(V_f)^3\right] \tag{11}$$

and

$$\zeta_f = 3-4\upsilon_{12f} \tag{12}$$

$$\zeta_m = 3-4\upsilon_m \tag{13}$$

The transversal Poisson's ratio ν_{23} is then obtained from the Hooke's law for transversely isotropic materials [22] as follows:

$$G_{23} = \frac{E_2}{2(1+\upsilon_{23})} \tag{14}$$

2.3.2 Meso-mechanical modeling

The tow architecture is discretized in the mesoscale. The material parameters from the microscale are used to characterize the fiber bundles which are modeled as homogenized continua. The textile architecture is described with a representative volume element (RVE) for reasons of numerical efficiency [16]. The final objective is to determine the material properties of one lamina for the macroscale level. Existing models are divided into two main categories: analytical and numerical models.

Early work on analytical modeling of woven composites was performed by Ishikawa and Chou [23] based on Classical Laminate Theory (CLT). They proposed the so-called mosaic model, which idealized the RVE as an arrangement of asymmetric cross-ply laminates and assumed a constant stress or strain condition in order to homogenize the mechanical properties. The prediction of the stiffness of the laminate is not complete because the model ignored the yarn crimp and the through thickness shear deformation. The fiber undulation model [24] was extended to consider fiber continuity and undulation in the longitudinal direction but neglected the transverse dimension. The undulation model was further refined by Naik and Ganesh [25] with a two-dimensional model which accounted for undulations in both the warp and weft directions. The RVE was fully described taking into account the cross-section geometry of the yarn, however, the model was only valid for the case of plain

weaves and the overall stiffness properties were obtained by assuming again either iso-stress or iso-strain conditions throughout the RVE. Many other models were derived from this concept. The discretization of the RVE is often refined and the method is generalized to more interlacing patterns. Special mention is deserved by Scida et al. [26] and Adumitroaie and Barbero [14] for developing one of the few methods to also predict the strength of woven fabric composites. However, they only consider uniaxial in-plane loading.

Given that the above mentioned analytical models are based on the fundamental assumptions used within the CLT, the prediction of three-dimensional properties lack any accuracy for thin laminates [3]. Furthermore, their simplicity does not allow to consider the stress concentrations which exist as a result of both external loads and complex 3D fabric architecture. Therefore, the use of numerical models will be necessary in order to deal with bending properties, micro-effects and damage onset.

Prodromou et al. [27] developed a model that falls between the analytical and finite element categories. This model is an implementation of the cell method originally formulated by Aboudi [28]. The stress field is obtained by minimizing the complementary energy function. Thus, the method does away with the constant stress/strain assumption and allows the prediction of stiffness and strength with better accuracy than the analytical methods, but not as well as the finite element models. Its greatest limitation is that it is not applicable for strength and failure prediction in multiaxial loading conditions.

Numerical models are based on the Finite Element Method (FEM) and their complexity depends on the geometrical description of RVE. The simplest way is by using 1D truss elements to represent the yarns. The first work on this subject was performed by Cox et al. [29] with the so-called binary model. This method has shown to provide good results for in-plane stiffness properties with low calculation cost. Soykasap [3] proposed beam elements to also study the bending stiffness. However, both techniques do not provide detailed insight into the stress field in the RVE since the actual yarn cross-section is not considered.

A 3D solid model of the RVE would therefore be the best approach for investigating both the stiffness and strength properties of fabric composites. A major drawback is the complexity of modeling and meshing the fabric geometry. A flexible modeling framework is the use of textile-oriented CAD tools such as WiseTex or TexGen, which have demonstrated to work well for woven composites [30, 31]. However, they present issues of yarn intersections that need to be carefully addressed when creating the geometry. For example, the yarn cross-sections and rotations may need to be adjusted to remove intersections. A gap between yarns may also be specified for this purpose, but special attention is needed to ensure the correct fibre volume fractions [32].

Although it is practically impossible to model the exact geometry, special care should be taken as stress concentrations will depend on it. It is common to extrapolate the weave geometry from the dry fabric by considering a constant elliptical section yarn. This shape approximation has been used thoroughly in the literature [14, 33, 34]. However, micrographs are recommended by many authors such as Mallikarachchi and Pellegrino [35] in order to measure the actual geometric properties of the impregnated fabric.

Many authors have used three-dimensional finite element models to predict the mechanical properties of woven composites. The required computation times have been minimized by using boundary conditions that take advantage of the symmetry and periodicity of the RVE [36]. The stresses and strains in the elements are related to the external loads applied on the RVE in order to obtain the homogenized material properties. However, most of the existing models for prediction of the strength only consider in-plane uniaxial loads [37, 38, 39] or, at most, biaxial loads [20, 33]. It is obvious that multiaxial loading presents a great increase in modeling complexity.

Karkkainen and Sankar [40] presented a direct micromechanics method (DMM) to determine the constitutive relations and failure initiation for textile composites. The RVE is modelled as a linear-elastic thin Kirchhoff plate which is subjected to force and moment resultants. The constitutive relationship is therefore written in the form of the ABD matrix. Thus, multiaxial loading is considered since any load can be defined as a combination of force and moment resultants. Rather than making assumptions based upon uniform stress or strain, the constitutive properties are obtained by averaging the micro-stresses over the entire RVE. The micro-stresses are used to predict the failure of the yarns or matrix by using well known failure criteria such as the maximum stress and Tsai-Wu. It is undoubtedly the best existing option to capture the unique characteristics of tape springs made out of woven composites. A more detailed explanation of this approach is presented in Section 3.2.

2.4 Failure Criteria

Common failure criteria developed for UD composites cannot be extended to model failure in macroscopic textile composite structures because they do not capture the unique characteristics intrinsic to textile geometry. However, they can be used to predict failure of the yarns or matrix at the mesoscale level. Karkkainen and Sankar [40] suggests the maximum principal stress criterion for the isotropic matrix and the Tsai-Wu failure criterion for the orthotropic fiber tows. It is noteworthy to mention that micro-stresses in the tows must be transformed in the warp and weft local coordinate systems (see Figure 3) in order to properly apply the corresponding failure criterion.

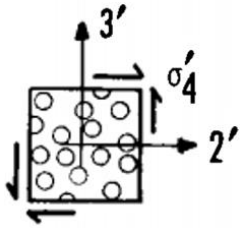

Figure 3. Stress components in the fiber tow-symmetry axes [41]

According to Kassapoglou [42], the maximum stress failure criterion compares the principal stresses induced in the material with their corresponding strength values as follows:

$$\begin{aligned} \sigma_1, \sigma_2, \sigma_3 &< \sigma_{ult}^t \\ \sigma_1, \sigma_2, \sigma_3 &> \sigma_{ult}^c \\ |\tau_{12}|, |\tau_{13}|, |\tau_{23}| &< S \end{aligned} \tag{15}$$

where σ_{ult}^{t}, σ_{ult}^{c}, and S are tension, compression and shear strength of the material, respectively. Failure will therefore occur as soon as one of the left-hand sides equals the right-hand side.

The form of the Tsai and Wu [41] failure criterion for 3-dimensional transversely isotropic materials is:

$$F_1\sigma_1' + F_2(\sigma_2' + \sigma_3') + F_{11}\sigma_1'^2 + F_{22}(\sigma_2'^2 + \sigma_3'^2 + 2\sigma_4'^2) + F_{66}\left(\sigma_5'^2 + \sigma_6'^2\right) + 2F_{12}(\sigma_1'\sigma_2' + \sigma_1'\sigma_3') + 2F_{23}(\sigma_2'\sigma_3' - \sigma_4'^2) \leq 1 \tag{16}$$

where F_i and F_{ij} are strength tensors of the second and fourth rank, which expressed in terms of engineering strengths are as follows [41]:

$$F_i = \begin{Bmatrix} \frac{1}{X^t} - \frac{1}{|X^c|} \\ \frac{1}{Y^t} - \frac{1}{|Y^c|} \\ \frac{1}{Y^t} - \frac{1}{|Y^c|} \\ 0 \\ 0 \\ 0 \end{Bmatrix} \tag{17}$$

$$F_{ij} = \begin{Bmatrix} \frac{1}{X^t|X^c|} & F_{12} & F_{12} & 0 & 0 & 0 \\ & \frac{1}{Y^t|Y^c|} & F_{23} & 0 & 0 & 0 \\ & & \frac{1}{Y^t|Y^c|} & 0 & 0 & 0 \\ & & & 2\left(\frac{1}{Y^t|Y^c|} - F_{23}\right) & 0 & 0 \\ & & & & \frac{1}{S^2} & 0 \\ & & & & & \frac{1}{S^2} \end{Bmatrix} \tag{18}$$

where:

- X^t is the tension failure along the fibers
- X^c is the compression failure along the fibers
- Y^t is the tension failure transverse to the fibers
- Y^c is the compression failure transverse to the fibers
- S is the pure shear failure

The interaction strength terms F_{12} and F_{23} are unfamiliar quantities that have to be determined experimentally using combined stress tests which are neither common nor straightforward. Assuming there will be no failure under practical levels of hydrostatic and equal transverse compression, DeTeresa and Larsen [43] derived the following relations in terms of the uniaxial strength parameters:

$$F_{12} = -\frac{F_{11}}{4} \tag{19}$$

$$F_{23} = -F_{22} \tag{20}$$

Thus, the Tsai-Wu failure criterion becomes:

$$F_1\sigma_1' + F_2(\sigma_2' + \sigma_3') + F_{11}\sigma_1'\left[\sigma_1' - \frac{1}{2}(\sigma_2' + \sigma_3')\right] + F_{22}(\sigma_2'^2 + \sigma_3'^2 - 2\sigma_2'\sigma_3' + 4\sigma_4'^2) + F_{66}(\sigma_5'^2 + \sigma_6'^2) \leq 1 \tag{21}$$

The failure mechanics of textile composites is particularly complex under multi-axial loading due to the stress gradient effects through the representative volume element (RVE). Karkkarinen et al. [44] developed an analytical expression to predict failure initiation with the ability to fit any general plate loading condition. The expression is based on the quadratic interactive nature of the stress state but written in terms of force and moment resultants as shown below:

$$C_{ij}F_iF_j + D_iF_i = 1 \tag{22}$$

where:

- F_i are the general load terms N_x, N_y, N_{xy}, M_x, M_y, and M_{xy}.
- C_{ij} and D_i represent 27 failure coefficients that accounts for the relative influence of each load as well as the interactions between them. Specifically, the terms D_i and C_{ii} correspond to uni-axial loading conditions, while the coefficients C_{ij} with $i \neq j$ relate to coupling between different loads.

The 27 failure coefficients can be reduced to 16 in case of symmetric woven composites, such as plain or twill weaves, because the strengths in both principal directions are the same. Furthermore, Karkkarinen et al. [44] state that coefficients D_3 through D_6 are equal to zero since failure values should not depend on the sign of the shear, moment, or twist loads. Mallikarachchi and Pellegrino [45] go further and state that the failure moment of an axially loaded plate should also be independent of the bending direction, which sets $C_{ij} = 0$ for $i = 3,...,6$ or $j = 3,...,6$ when $i \neq j$. All the stated symmetry conditions above reduce the number of failure coefficients to only 6 and thus the quadratic failure criterion in Equation (22) becomes:

$$D_1(N_x + N_y) + C_{11}(N_x^2 + N_y^2) + C_{12}N_xN_y + C_{33}N_{xy}^2 + C_{44}(M_x^2 + M_y^2) + C_{66}M_{xy}^2 = 1 \tag{23}$$

Mallikarachchi and Pellegrino [45] performed experimental tests for two-ply plain weave CFRP laminates under combined loading in order to evaluate the accuracy of the failure criterion presented by Karkkarinen et al. [44]. It was observed that the axial-bending interaction was not quadratic and that many of the experimentally determined failure points lie inside the N_x - M_x failure envelope (Figure 4).

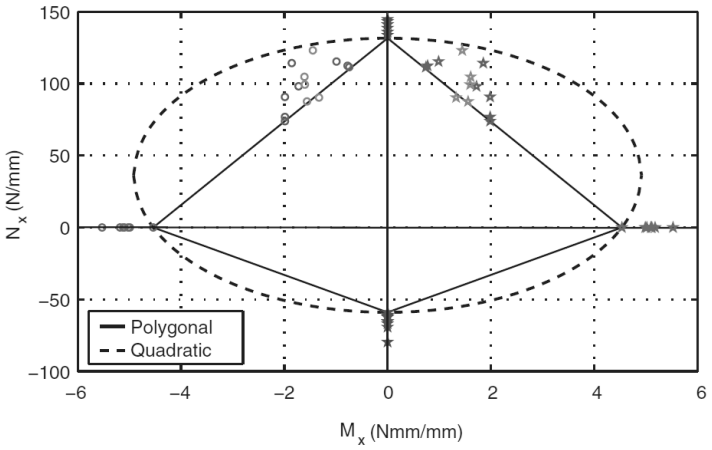

Figure 4. Axial-bending interaction for a two-ply plain weave composite [45]

It can be seen from Figure 4 above that a polygonal criterion would be more appropriate to describe the interaction between N_x and M_x. Therefore, Mallikarachchi and Pellegrino [45] proposed an alternative failure criterion inspired by experimental observations that considers the following three projections:

- Failure under pure in-plane loading, see Equation (24).
- Failure under biaxial bending, see Equation (25).
- Failure due to the interaction between in-plane and bending loads, see Equation (26).

In the case of in-plane loading, failure is satisfactorily defined by the original quadratic form, and thus Equation (22) reduces to:

$$D_1(N_x + N_y) + C_{11}(N_x^2 + N_y^2) + C_{12}N_xN_y + C_{33}N_{xy}^2 < 1 \tag{24}$$

Experimental results presented by Yee [46] and Mallikarachchi and Pellegrino [45] show that the value of M_x at failure is practically independent of M_y for thin plain weave laminates. Hence, it is assumed that only the maximum of the two bending moments leads to failure under biaxial bending. The failure limits for bending and twisting loads can therefore be defined as follows:

$$\begin{aligned} C_{44}M_x^2 + C_{66}M_{xy}^2 &< 1 \\ C_{44}M_y^2 + C_{66}M_{xy}^2 &< 1 \end{aligned} \tag{25}$$

In the case of combined in-plane and bending loading, the experimental tests show that axial failure does not change when a moment is applied in transverse direction. Similarly, the shear strength does not change in the presence of a twisting moment. Thus, Mallikarachchi and Pellegrino [45] concluded that the only significant interaction is between in-plane and bending resultants applied in the same direction. As previously mentioned, a quadratic failure criterion does not perfectly work in this case and the following linear interaction is assumed:

$$\begin{aligned} \frac{N_x}{F_x} + \sqrt{C_{44}} \cdot |M_x| &< 1 \\ \frac{N_y}{F_y} + \sqrt{C_{44}} \cdot |M_y| &< 1 \end{aligned} \tag{26}$$

where F_x and F_y are the axial failure strengths given by:

$$F_x = \frac{-(D_1 + C_{12}N_y)}{2C_{11}} \pm \frac{\sqrt{(D_1 + C_{12}N_y)^2 - 4C_{11}(D_1N_y + C_{11}N_y^2 + C_{33}N_{xy}^2 - 1)}}{2C_{11}}$$
$$F_y = \frac{-(D_1 + C_{12}N_x)}{2C_{11}} \pm \frac{\sqrt{(D_1 + C_{12}N_x)^2 - 4C_{11}(D_1N_x + C_{11}N_x^2 + C_{33}N_{xy}^2 - 1)}}{2C_{11}} \quad (27)$$

It is important to note that failure by delamination was not taken into account in the proposed failure criterion. However, this failure mode was not visible in any of the strength measurement tests performed by Mallikarachchi and Pellegrino [45].

Chapter 3 Unit Cell Analysis of Textile Composites

This chapter presents the modelling techniques that have been used for the analysis of woven composites. The different characteristics between plain and twill patterns will be studied, as well as the peculiarities of ultra-thin composites. This section will allow to validate the methodology that will be later used for the analysis of the tape-springs made out of ultra-thin laminates. The unit cell approach is explained in detail. First, the generation and discretization of the textile geometry is addressed for each case study. Second, the methodology to estimate the mechanical properties and the failure initiation is described. The plain and twill models are subjected to in-plane pure tension load in order to understand the mechanisms of failure initiation and compared the results against experimental data. Finally, the ultra-thin model is subjected to more complex loads, such as shear or bending, to better represent the loading conditions that will be encountered in tape-springs.

3.1 Unit Cell Generation

The unit cell or representative volume element (RVE) is the smallest possible building block needed to represent the textile composite [31]. The periodic structure of woven composites makes possible to evaluate the homogenized mechanical properties just by using an RVE of the entire composite. A realistic model of the RVE geometry is therefore essential for a reliable prediction. However, the complex weave architecture of textile composites makes the RVE modeling extremely challenging.

The RVE is modeled as a rectangular cuboid with the dimensions of the repetitive textile pattern. The modeling of the yarns is the main challenge since the matrix is assumed to fill the volume left in the cuboid. The open source software TexGen [47] has been used to create the textile geometry. TexGen defines the yarn path as a cubic spline based on certain input parameters such as weave pattern and yarn dimensions. The textile models usually present issues of local interpenetrations of the yarns, which need to be carefully addressed when creating the geometry.

An additional difficulty is how to discretize the RVE from the textile geometry. A mesh with tetrahedral shaped elements may present distorted elements between the yarns, which increase solution error. This drawback can be solved by using a voxel mesh, which is formed by a regular grid of cubic elements where non-orthogonal interfaces are stepped. The aspect ratio is defined a priori, but artificial stress concentrations will appear as a consequence of the stepped geometry [48]. Although this spurious effect is relatively benign for elastic stiffness characterization, it will have a significant impact for prediction of damage initiation. To overcome this limitation, Fang et al. [49] proposed a post-processing stress averaging technique to alleviate local artificial stresses. However, the most correct solution would be using a mesh with tetrahedral or hexahedral shaped elements, which is a

difficult task due to the lack of capability of most existing auto-meshing softwares to generate a periodic mesh for complex geometries.

3.1.1 Plain Woven Composite

A plain weave laminate [50] with no layer shift has been the first composite chosen for the validation study. Plain woven composites have the simplest RVE with only two warp and two weft yarns, thus it is the most appropriate weave style to start investigating the geometric and meshing generation issues mentioned above. First of all, the following parameters are required by TexGen in order to construct the unit cell of a woven composite:

- Width and height of yarns
- Yarn spacing
- Ply thickness
- Weave pattern

The parameters above can be obtained by using an optical microscope. Ito and Chou [50] performed an experimental study of the plain weave composite and Matveev [32] used their microscopic observations to model the textile geometry with TexGen. The geometric parameters and composite details are given in the following table:

Table 1. Parameters of plain weave composite [32]

Plain Weave	
Fibre volume fraction, %	42
Laminate thickness, mm	4.99
Number of layers	8
Warp/weft spacing, mm	3.14
Warp/weft width, mm	2.97
Warp/weft yarns	12K AS4 carbon fiber
Matrix	Vinyl ester (Dow DERAKANE 411-C-50)

TexGen has a Graphical User Interface to describe the weaving pattern and create the geometry by using the parameters shown in Table 1. This procedure can be very time-consuming, as the textile geometry needs to be entirely redefined to apply any small modification. Therefore, the models were generated using Python, which is embedded in the TexGen GUI and allows easy access to every functionality.

The yarns were initially defined by considering a constant lenticular cross-section, but they presented multiple local interpenetrations. This problem was attempted to be solved by introducing an artificial gap between the yarns. However, the resulting models were not realistic since the unit cell thickness had to be increased. Furthermore, this approach requires several trial and error attempts, which makes it infeasible. The yarn interference issues have been solved by using a built-in TexGen algorithm which allows to automatically adjust local rotations and changes of cross-sections to remove the interpenetrations [51]. The resulting plain woven geometry and dimensions of the unit cell are shown in the following Figure 5.

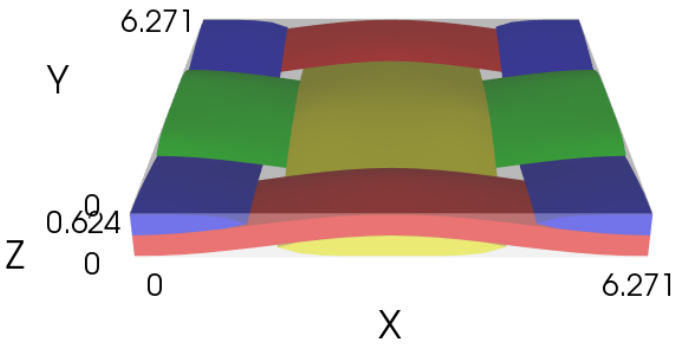

Figure 5. Representative volume element of plain woven composite generated with TexGen

The next step is to discretize the RVE geometry, which is a complex task due to the small gaps between the yarns. The simplest strategy to discretize the model is creating a voxel-based mesh using TexGen. However, this technique has important drawbacks. The first one is that a very high number of elements is required to capture all of the detail in the textile, which is limited by the computational demand. The second drawback is related to the artificial stress concentrations induced due to the block-like representation of the tow/matrix interface surfaces [48]. This effect needs to be avoided for failure prediction where local stresses play an important role, especially under multi-axial loading conditions. Figure 7 shows that the stepped geometry cannot be avoided even when a large number of voxel elements is used.

A conformal mesh would therefore be the best option to discretize the textile geometry, but the meshing process is more difficult to implement for general geometries. The first approach tried was to import the textile geometry as a .STEP file into Abaqus for creating a tetrahedral-based mesh. The importing process often fails due to an *imprecise geometry* error from Abaqus, which cannot always be solved by repairing the geometry. Furthermore, this approach was discarded because the mesh usually contains elements with unacceptable aspect ratios in regions between yarns.

The second approach was to create the tetrahedral mesh using the algorithm TetGen [52] implemented in TexGen. The software has a merge tolerance option that allows to reduce the bad quality elements between yarns. Although this approach is found to be robust, the major problem is that nodes are not always coupled on opposite sides of the RVE as is required when periodic boundary conditions has to be applied. However, this problem has been overcome by using a novel methodology to apply periodic BCs (see Section 3.2.1.). Hence, the latter approach has been found to be the most appropriate solution to generate a tetrahedral mesh for an arbitrary woven composite RVE. Figure 6 below shows the resulting mesh for the plain woven geometry previously defined.

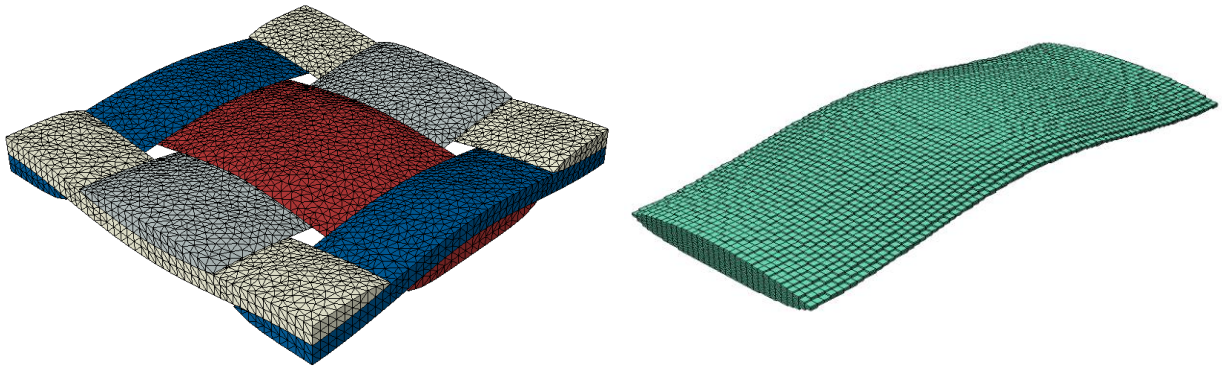

Figure 6. Tetrahedral-based (left) and voxel-based (right) mesh

3.1.2 Twill Woven Composite

The twill woven laminate chosen for validation was manufactured by Matveev [32] imposing no layer shift. Micro-CT analysis were used to measure the impregnated textile geometry. The parameters required to create the unit cell model using TexGen are listed in Table 2.

Table 2. Parameters of twill weave composite [32]

Twill Weave	
Fibre volume fraction, %	55
Laminate thickness, mm	4.0
Number of layers	6
Warp/weft spacing, mm	2.5
Warp/weft width, mm	2.5
Warp/weft yarns	12K Grafil 34-700 carbon fibre
Matrix	Epoxy resin (Gurit Prime 20LV)

The twill weave style is done by passing two warp yarns every two weft yarns, which makes the unit cell geometry more complex than for plain woven composites. The micro-CT images showed that the rotations of the yarn's cross-section is much more pronounced. This effect has been captured by using the automatic geometry refinement implemented in TexGen. The resulting model of the unit cell is shown in Figure 7 below.

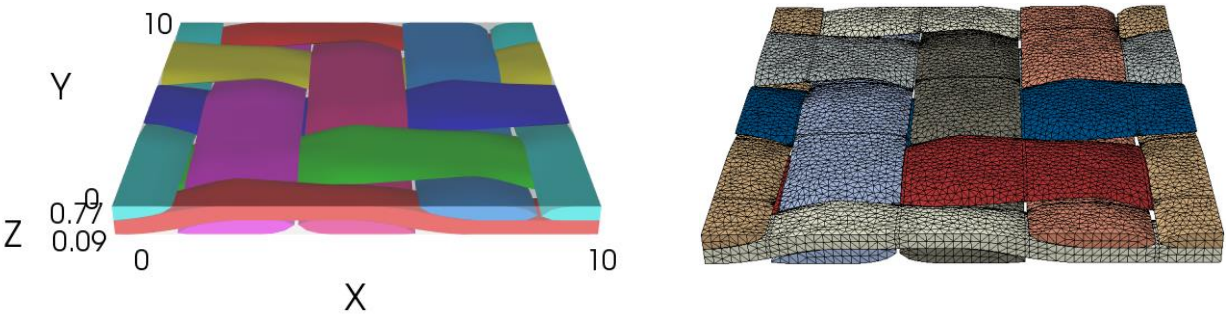

Figure 7. Representative volume element of twill woven composite

The discretization of the textile geometry was performed as described above for the plain weave. It is important to note that the number of elements required for mesh convergence increases considera-

bly due to the larger size of the unit cell. TexGen has the option to export linear or quadratic tetrahedral elements. As it is described in Section 3.3.2, it has been observed that second order elements give better predictions when out-of-plane loads are present. However, the option to export them sometimes causes distorted elements. Hence, linear tetrahedral elements has been chosen to create the mesh with Texgen, and the Abaqus software has subsequently been used to modify the element order.

3.1.3 Ultra-thin Plain Weave Composite

The models to validate the unit cell approach under tensile loading for both plain and twill weaves have been presented above. However, additional validation is still necessary for out-of-plane loading of ultra-thin woven composites since these conditions will be given in the tape-springs. Almost no research has been conducted on this subject, thus experimental data is hardly available.

Mallikarachchi [35] carried out a series of tests to characterize the membrane and bending stiffness properties of a two-ply T300/Hexcel 913 plain weave laminate. Micrographs were also performed to determine the geometrical properties of the yarns. An example of micrograph taken is shown in Figure 8. Full details of the weave architecture were not measured, but the most important average values were given as shown in Table 3.

Table 3. Average geometric properties of a T300/HexPly913 tow [35]

Laminate thickness, mm	0.22
Weave length, mm	2.664
Maximum tow thickness, mm	0.059
Tow cross-sectional area, mm^2	0.0522

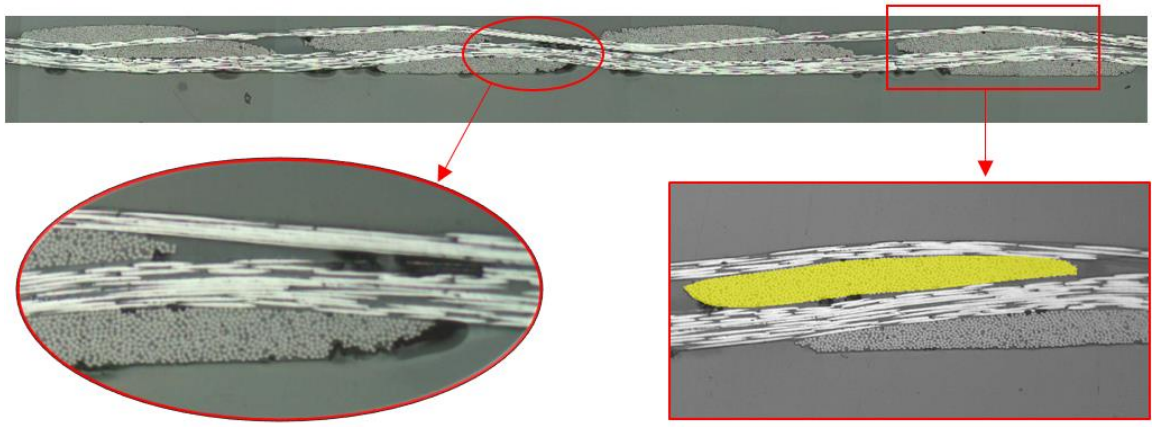

Figure 8. Micrograph of T300/913 two-ply plain weave laminate [35]

Mallikarachchi [35] used Autocad software to measure the geometric properties of four different specimen. Alternatively, the cross-sectional area of a yarn has been measured using the Image Segmenter Toolbox in Matlab in order to compare the result and validate future measurements performed in tape-spring samples. The toolbox allows to measure the dimensions in pixels, which can be scaled to mm by using the scale bar given by the micrographs. The tow cross-sectional area obtained with Matlab is A = 0.0508 mm^2, which is in very good agreement with the average value presented in Table 3.

An important observation is the amount of voids existing in the composite specimen. A detail image is shown in Figure 8. The void content between yarns is significant even though the samples were cured in an autoclave. It is important to note the amount of resin gaps existing in the bottom part of the micrograph, while the top part is free of them. This effect has also been observed in the tape-spring samples, which were initially manufactured by using a vacuum bag. Mallikarachchi [35] used the same method to produce composite tubes, which is schematically illustrated in Figure 9 below:

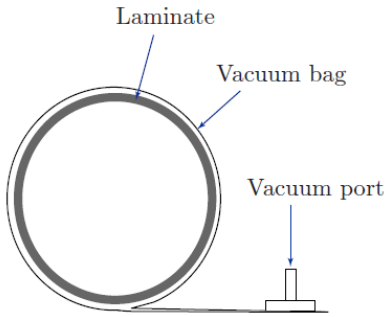

Figure 9. Vacuum bagging technique to produce composite tubes [35]

It has been observed that the tape-springs produced with this technique present high waviness at the surface in contact with the vacuum bag. Therefore, a different technique with two rigid molds has been finally chosen in order to avoid this undesirable effect and obtain perfectly flat surfaces.

Unlike the plain and twill woven composites presented before, shift layer was not controlled during the manufacturing process of the two-ply laminate studied in this section. This is also the case for the tape-spring samples manufactured by Thales Alenia Space, thus it is an important factor to take into account. As it can be seen from the micrograph shown in Figure 8, it seems as if the tows tend to interpenetrate the adjacent layer rather than staying in an iso-phase configuration.

Three different models were created in order to study the effect of the layer shift. The following three extreme configurations were considered: layers in-phase, π/2 out-of-phase, and π/4 out-of-phase. The unit cells were created using TexGen assuming that both reinforcement and matrix occupy all the volume with no voids. However, the fibre volume fraction has been estimated as detailed in Section 3.2.2 by considering this assumption.

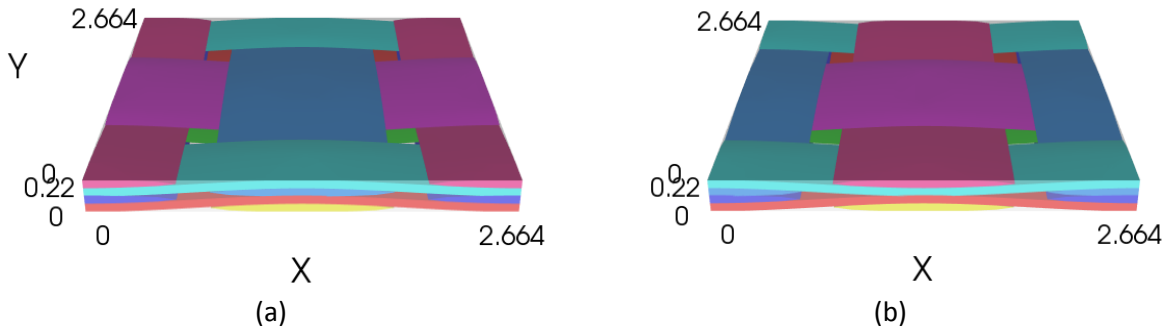

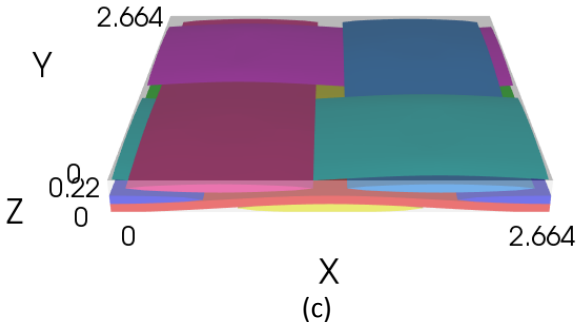

(c)

Figure 10. Three extreme ply configurations; (a) fibers in-phase, (b) fibers π/2 out-of-phase, (c) fibers π/4 out-of-phase

3.2 Finite Element Micromechanics Method

3.2.1 Periodic Boundary Conditions

For the homogenization of the mechanical properties it is necessary to apply certain boundary conditions to the RVE. Different options have been proposed in the literature, such as the Dirichlet, Mixed, and Periodic boundary conditions. However, only periodic boundary conditions satisfy the periodicity of the stress-strain field. The RVE must be mechanically repeatable to ensure continuity of micro-stresses and compatibility of displacements, which means having equal response to strains and curvatures for every location of the RVE [53, 40].

The periodic boundary conditions have to be applied by linearly constraining the displacements of paired nodes on opposite sides of the RVE. The expression for two arbitrary nodes A and B can be written as follows:

$$\mathbf{u}^{\mathrm{A}} = \mathbf{u}^{\mathrm{B}} \tag{28}$$

An additional term needs to be added to Equation (28) above in order to simulate an applied macroscopic load and thus evaluate the homogenized properties of the RVE. For this, opposite nodes of the unit cell can be subjected to a relative displacement as follows:

$$\mathbf{u}^{\mathrm{A}} - \mathbf{u}^{\mathrm{B}} = \varepsilon \cdot \mathrm{d} \tag{29}$$

where ε is the applied strain and d is the distance between opposite nodes.

Karkkainen and Sankar [40] developed a micromechanics method in which individual unit strains and curvatures are applied to the unit cell in order to evaluate the stiffness [ABD] matrix. Figure 11 and Table 4 below shows the appropriate boundary conditions when each independent macroscopic unit deformation is applied.

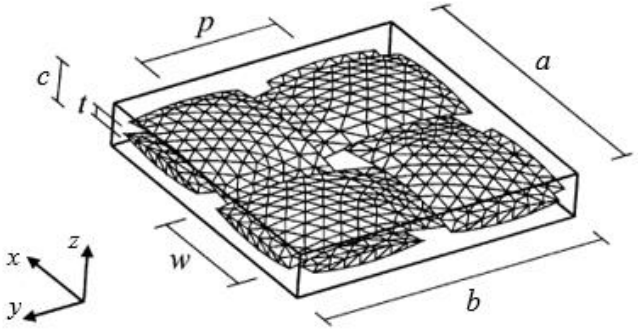

Figure 11. RVE geometry definition [40]

Table 4. Periodic displacement boundary conditions [40]

		$u(a,y)-u(0,y)$	$v(a,y)-v(0,y)$	$W(a,y)-W(0,y)$	$u(x,b)-u(x,0)$	$v(x,b)-v(x,0)$	$w(x,b)-w(x,0)$
1	$\varepsilon_x^M=1$	a	0	0	0	0	0
2	$\varepsilon_y^M=1$	0	0	0	0	b	0
3	$\gamma_{xy}^M=1$	0	$a/2$	0	$b/2$	0	0
4	$\kappa_x^M=1$	az	0	$-a^2/2$	0	0	0
5	$\kappa_y^M=1$	0	0	0	0	bz	$-b^2/2$
6	$\kappa_{xy}^M=1$	0	$az/2$	$-ay/2$	$bz/2$	0	$-bx/2$

The displacement boundary conditions defined by Karkkainen and Sankar [40] should be applied for thin woven composites where multi-axial loading conditions are present. However, it is important to note that these periodic BCs are applied only in the in-plane direction and not through-thickness direction, as this would alter the bending stiffness and bending extension coupling. Thus, the top and bottom faces of the unit cell are under stress free conditions. Periodic BCs should be applied in all three directions (see Figure 12) for a single-layer model where periodic geometry exists through-thickness direction. However, the latter approach assumes that the unit cell is embedded in an infinite medium in all three coordinate directions. Hence, it neglects any possible edge effect, which may have a severe impact on thin-laminates. The effect of both models will be explored in Section 3.3.1.

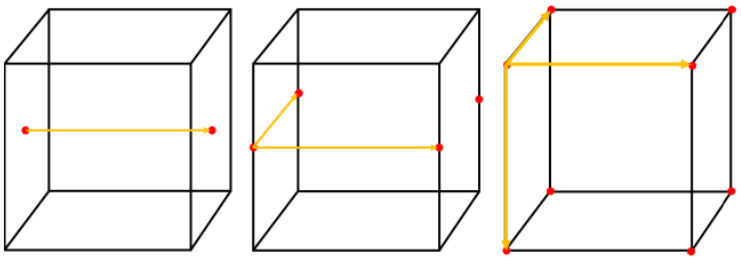

Figure 12. Periodic connectivity of nodes in all three directions on a simple cubic domain boundary

A periodic mesh on the external domain boundary of the unit cell is necessary to define the periodic boundary conditions. This means that node positions on opposite boundaries should have an exact 1:1 correlation. However, as it has been pointed out in Section 3.1.1, a different approach has been adopted since it is not straightforward to create a conformal mesh for a textile geometry with the nodes perfectly coupled. The nodes from one face were copied to the opposite face and the surface-to-surface ties in Abaqus were used to constrain the copied nodes to the underlying RVE mesh. Finally, the periodic relationships were imposed between the nodes on the original and the copied face.

This approach has been carried out by using a novel Micromechanics Plugin developed for Abaqus 2017.

3.2.2 Unit Cell Homogenization

In the micromechanics method [40], each applied macroscopic unit strain and curvature results in a detailed map of RVE micro-stress fields. In the same way, each case will correspond to a certain macro force and moment resultant that can be obtained as follows:

$$N_{ij} = \frac{1}{ab}\sum \sigma_{ij}^{e} V^{e} \tag{30}$$

$$M_{ij} = \frac{1}{ab}\sum z\sigma_{ij}^{e} V^{e} \tag{31}$$

where *a* and *b* are the dimensions of the unit cell as indicated in Figure 11, V^e is the element volume, and σ_{ij}^{e} is the microstress tensor of each element.

Thus, the constitutive [A], [B] and [D] matrices of Equation (2) can be evaluated by independently applying the six load conditions shown in Table 4. Based on these results, the laminate stiffness properties in all directions can be calculated using the following relations [42].

$$\begin{aligned} E_{1m} &= \frac{1}{ha_{11}} & E_{1b} &= \frac{12}{h^3 d_{11}} \\ E_{2m} &= \frac{1}{ha_{22}} & E_{2b} &= \frac{12}{h^3 d_{22}} \\ G_{12m} &= \frac{1}{ha_{66}} & G_{12b} &= \frac{12}{h^3 d_{66}} \\ \upsilon_{12m} &= -\frac{a_{12}}{a_{22}} & \upsilon_{12b} &= -\frac{d_{12}}{d_{22}} \\ \upsilon_{21m} &= -\frac{a_{12}}{a_{11}} & \upsilon_{21b} &= -\frac{d_{12}}{d_{11}} \end{aligned} \tag{32}$$

where *h* is the thickness of the laminate, [a] = $[A]^{-1}$ and [d] = $[D]^{-1}$. It is important to note that these equations are valid only for symmetric laminates where the coupling matrix [B] is zero, which is a necessary requirement for bi-stable tape springs as discussed in Section 2.2.

The mechanical properties of a simple isotropic plate has been calculated by using the micromechanics approach explained above. Results have been compared with the Classical Laminate Theory in order to validate the method. The model used has been the unit cell created for the plain woven composite in Section 3.1.1. Matrix and yarns were both defined as isotropic materials with Young's modulus E = 3450 MPa and Poisson's ratio ν = 0.35. The results for each independent macroscopic unit strain and curvature are shown in Figure 13 below.

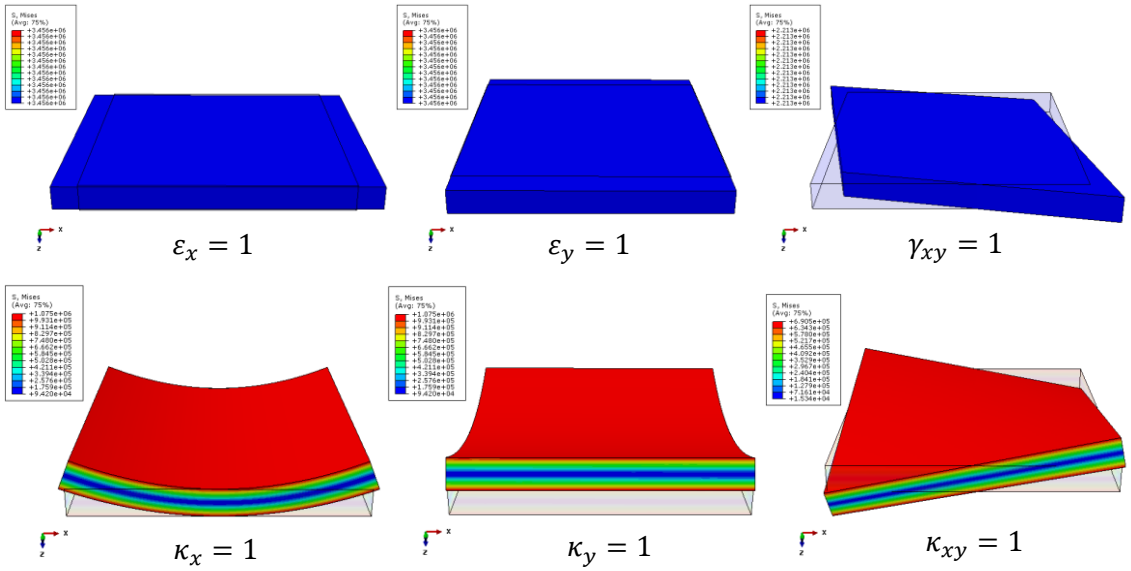

Figure 13. Stress field for the six independent unit deformations

The ABD stiffness matrix is then calculated by using Equations (30) and (31). The integration point stresses and the volume associated with each corresponding integration point have been used in order to average the micro-stresses over the entire RVE. The following result was thus obtained:

$$[A] = \begin{bmatrix} 2453 & 858.7 & 0 \\ 858.7 & 2453 & 0 \\ 0 & 0 & 797.3 \end{bmatrix} MPa - mm$$

$$[B] = \begin{bmatrix} 0 & 0 & 0 \\ 0 & 0 & 0 \\ 0 & 0 & 0 \end{bmatrix} MPa - mm^2$$

$$[D] = \begin{bmatrix} 80.05 & 27.84 & 0 \\ 27.84 & 80.05 & 0 \\ 0 & 0 & 25.88 \end{bmatrix} MPa - mm^3$$

The ABD matrix has also been calculated using the Classical Laminate Theory [42]. First of all, the stiffness matrix Q for an isotropic thin-plate under plane stress is given as follows:

$$\begin{Bmatrix} \sigma_x \\ \sigma_y \\ \sigma_{xy} \end{Bmatrix} = \begin{bmatrix} \frac{E}{1-\nu^2} & \frac{\nu E}{1-\nu^2} & 0 \\ \frac{\nu E}{1-\nu^2} & \frac{E}{1-\nu^2} & 0 \\ 0 & 0 & \frac{E}{2(1+\nu)} \end{bmatrix} \begin{Bmatrix} \varepsilon_x \\ \varepsilon_y \\ \gamma_{xy} \end{Bmatrix} \quad (33)$$

Since the material is isotropic, there is not coupling between the membrane and bending deformations. Therefore, the membrane and bending response can be calculated by using the following equations:

$$A_{ij} = Q_{ij} h \quad (34)$$

$$D_{ij} = Q_{ij}\frac{h^3}{12} \tag{35}$$

The relative error between the analytical and numerical results is almost exactly zero, which validates the application of the periodic boundary conditions as well as the methodology used to calculate the [ABD] matrix of the RVE.

3.2.3 Unit Cell Failure Analysis

Failure initiation can be studied by using the element stresses obtained from the application of the six independent unit deformations described above. First, the micro-stress field resulting from any general macro deformation can be extrapolated as follows [40].

$$\begin{Bmatrix} \sigma_x \\ \sigma_y \\ \sigma_z \\ \tau_{yz} \\ \sigma_{xz} \\ \sigma_{xy} \end{Bmatrix}^e = [F]^e \begin{Bmatrix} \varepsilon_x^M \\ \varepsilon_y^M \\ \gamma_{xy}^M \\ \kappa_x^M \\ \kappa_y^M \\ \kappa_{xy}^M \end{Bmatrix} \tag{36}$$

where:

- $[F]^e$ is a 6 x 6 matrix that contains the six stress components in each element resulting from the six single unit macrostrain analysis.
- ε_M and κ_M are the macroscopic strain and curvature corresponding to a general applied force [N] or moment [M] resultant.

Failure is checked by applying a certain failure criterion to each element of the RVE while gradually increasing a selected macroscopic load. The macrostrains ε_M and curvatures κ_M are calculated using the ABD stiffness matrix obtained from the unit cell homogenization. The complete failure analysis procedure is summarized in the flow diagram shown in Figure 14, where *e* is the element number.

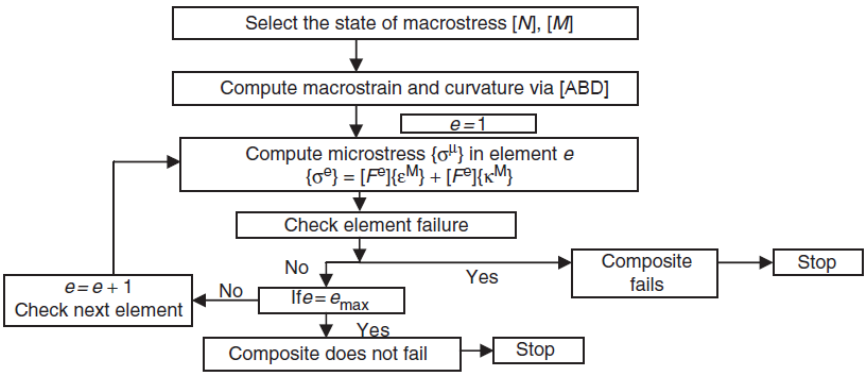

Figure 14. Flow diagram for failure analysis [40]

The yarns are assumed to be homogenous and transversely isotropic, thus any benchmarked failure criteria for UD composites could be used. Strength tensor based criteria such as Tsai-Wu are usually more suitable to predict failure of anisotropic materials subjected to complex stress states since it takes into account the interaction of biaxial stresses. However, they do not predict the damage

mode, which strongly affects the mechanisms of strength reduction [54]. Rujiter [55] proposed a modified maximum stress criterion to overcome this limitation. The criteria is based on the following damage variables:

$$D_1 = \max\left(\frac{\sigma_{11}}{S_{11}^t}, -\frac{\sigma_{11}}{S_{11}^c}\right) \tag{37}$$

$$D_2 = \frac{\sqrt{\sigma_{12}^2 + \sigma_{13}^2}}{S_{12}} \tag{38}$$

$$D_3 = \max\left(\frac{\max(\sigma_{22,}\sigma_{33})}{S_{22}^t}, -\frac{\min(\sigma_{22,}\sigma_{33})}{S_{22}^c}\right) \tag{39}$$

Failure initiation occurs when any of the three damage variables $D_i > 1$. Additionally, Ruijter [55] defined the following rule to model the stiffness degradation after the initiation of failure:

$$E_1 = E_1^0 \begin{cases} 1, & D_1 \leq 1 \\ 0.001, & D_1 > 1 \end{cases} \tag{40}$$

$$E_2 = E_3 = E_2^0 \max\big(0.001, \min\big(P(D_2), P(D_3)\big)\big) \tag{41}$$

$$G_{12} = G_{13} = G_{12}^0 \max\big(0.001, \min\big(P(D_2), P(D_3)\big)\big) \tag{42}$$

where

$$P(D_i) = 1 - \frac{1}{\exp(-c_1 D_i + c_2)} \tag{43}$$

where c_1 and c_2 are empirical constants.

Although damage propagation is out of the scope of the present work, the expressions above are very useful to understand damage initiation. As can be seen, it is assumed that damage in the fibers direction leads to catastrophic failure, while damage propagates gradually in the transverse direction. The advantage of this criterion with respect Tsai-Wu is the possibility to distinguish the modes of failure, which can be classified as shown in Figure 15. The mode L represents fibre failure; the modes T and Z represent transverse cracking; the others correspond to shear failure [54]. The failure analysis procedure has been implemented in Matlab as further detailed in the following Section 3.3.

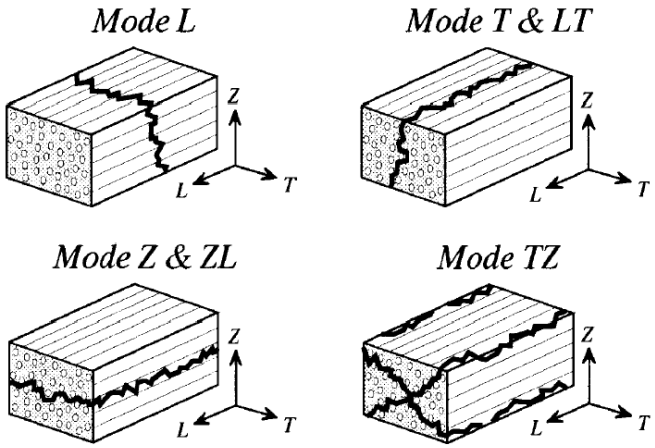

Figure 15. Damage modes for fibre bundles [54]

3.3 Numerical Results

This section is organized in two parts. The first one presents the results of the plain and twill models subjected to in-plane pure tension, and the second one presents the results of the ultra-thin woven model under in-plane and out-of-plane loading.

3.3.1 Tensile loading

The plain and twill models, presented respectively in Section 3.1.1 and Section 3.1.2, have been analyzed using the numerical unit cell approach and the results have been compared against experimental data from tensile tests. For simplicity, the modeling details are introduced by using the plain woven composite. First of all, the homogenized material properties used to define both matrix and yarns are listed in Table 5 below.

Table 5. Material properties of matrix and yarns for plain woven composite [32]

	E_{11}, GPa	$E_{22} = E_{33}$, GPa	$G_{12} = G_{13}$, GPa	G_{23}, GPa	$\nu_{12} = \nu_{13}$	ν_{23}	S_{11}, MPa	S_{22}, MPa	S_{12}, MPa
Vinyl ester	3.45	3.45	1.28	1.28	0.35	0.35	76	-	-
Yarns (V_f = 0.63)	140.5	10.6	7.9	3.11	0.285	0.349	2497	31.6	36

The material properties of the yarns are orthotropic, thus it is extremely important to assign the correct material orientation in the Abaqus model. For this purpose, the center points of the fiber tow elements are used to interrogate the TexGen model and extract the orientation information that is input in Abaqus. Figure 16 below shows the normals to the yarn path orientation.

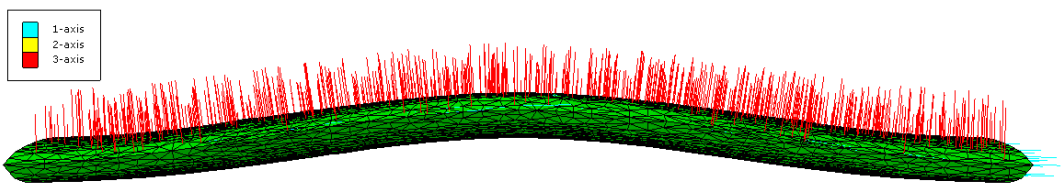

Figure 16. Material orientation vectors in a yarn

It is important to note that the plain weave laminate consists of 8 layers as shown in Table 1. However, the model has been simplified as a single-layer in order to reduce the computational effort. Two models have been created in order to study the effect of boundary conditions: a first one in which periodic BCs are applied in the in-plane direction and a second one where they are applied in all three directions. The unit cell homogenization has been performed as described in Section 3.2.2. The results obtained and the corresponding relative error are listed in Table 6 below.

Table 6. Homogenized Young's modulus of the plain woven composite

	Young's modulus, GPa	**Error, %**
Experimental value [50]	40.5 (2.12)	-
FE with periodic BCs in the in-plane direction	34.6	14.5
FE with periodic BCs in all three directions	42.5	4.9

The results show good agreement with the experimental data. It is observed that leaving the top and bottom faces of the unit cell are under stress free conditions leads to a relative error of 14.5%, while applying periodic BCs in through thickness direction reduces the error to 4.9%. As it has been explained in Section 3.2.1, periodic BCs in all three directions are more appropriate when modeling thick laminates as a single-layer. The plain woven composite was manufactured by imposing the exact same position for each layer [50], thus it is acceptable to assume that the unit cell is embedded in an infinite periodic medium in all three coordinate directions. This assumption neglects any possible edge effect, which might be the reason for the relatively small error. Slight variations in the geometry and material definition might also affect the result accuracy. The stress field for the longitudinal and transverse yarns are shown in Figure 17 below. The yarn elements have been isolated from the matrix in order to provide better insight. The longitudinal stresses S_{11} and transverse stresses S_{22} are shown for the longitudinal and transverse yarns, respectively, since they correspond with the maximum principal stresses. It can be seen that the critical locations are close to the edges at the intersection between the weft and warp yarns.

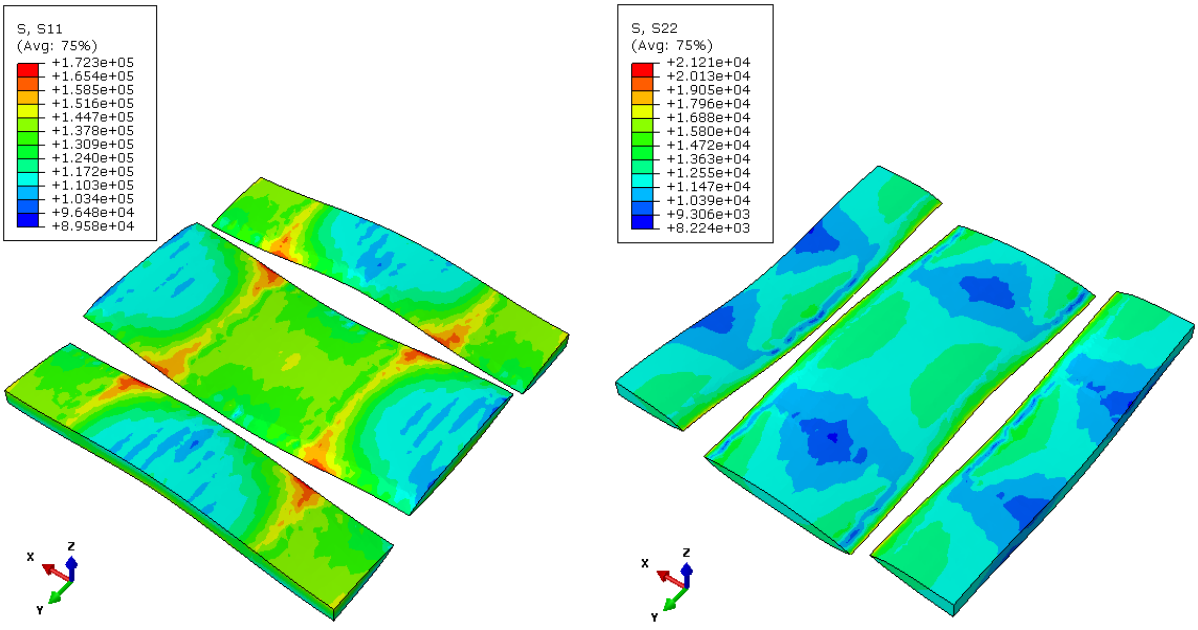

Figure 17. Stress field (MPa) for the longitudinal (left) and transverse (right) yarns for a unit strain applied in the x-direction

The six independent components of the stress tensor for each element were exported to Matlab in order to predict failure initiation due to tensile loading. It is important to note that the displacement in the transverse direction is not zero when the plain woven composite is loaded in the yarn directions. Hence, the stress field resulting from any tensile force has to be extrapolated by considering both longitudinal and transverse strains as follows:

$$\begin{Bmatrix} \boldsymbol{\sigma_x} \\ \boldsymbol{\sigma_y} \\ \boldsymbol{\sigma_z} \\ \boldsymbol{\sigma_{yz}} \\ \boldsymbol{\sigma_{xz}} \\ \boldsymbol{\sigma_{xy}} \end{Bmatrix}^e = \begin{bmatrix} \boldsymbol{\sigma_x}^{\varepsilon_x=1} & \boldsymbol{\sigma_x}^{\varepsilon_y=1} \\ \boldsymbol{\sigma_y}^{\varepsilon_x=1} & \boldsymbol{\sigma_y}^{\varepsilon_y=1} \\ \boldsymbol{\sigma_z}^{\varepsilon_x=1} & \boldsymbol{\sigma_z}^{\varepsilon_y=1} \\ \boldsymbol{\sigma_{yz}}^{\varepsilon_x=1} & \boldsymbol{\sigma_{yz}}^{\varepsilon_y=1} \\ \boldsymbol{\sigma_{xz}}^{\varepsilon_x=1} & \boldsymbol{\sigma_{xz}}^{\varepsilon_y=1} \\ \boldsymbol{\sigma_{xy}}^{\varepsilon_x=1} & \boldsymbol{\sigma_{xy}}^{\varepsilon_y=1} \end{bmatrix}^e \begin{Bmatrix} \boldsymbol{\varepsilon_x^M} \\ \boldsymbol{\varepsilon_y^M} \end{Bmatrix} \tag{44}$$

Damage onset can be studied using Matlab by gradually increasing the tensile force as described in Section 3.2.3. The resulting macrostrains are used to calculate the new components of the stress tensor for each element as shown in Equation (44). The modified maximum stress criterion presented in Section 3.2.3 has been used in order to understand the mechanisms of damage initiation. The criteria is applied on an element-by-element basis, which allows to detect the location of failure. For that, the input file (*.inp) generated by Abaqus was exported to Matlab in order to sort out the yarn and matrix elements. It is assumed that the yarn elements fail in the longitudinal direction when $D_1 > 1$. However, two different approaches have been considered for the definition of initial transverse failure of the yarns, as it is assumed that the elements would not abruptly collapse in this direction. The first one considers failure when $D_3 > 1$, see Equation (39), and will be referred as *Early Damage Initiation*. This definition will indicate the initiation of the first transverse micro-cracks, but it does not represent the complete failure of the element. The second one will be referred as *Damage Initiation* and it assumes that the element completely fails when the following expression is satisfied:

$$P(D_3) = 1 - \frac{1}{\exp(-c_1 D_3 + c_2)} \leq 0.001 \tag{45}$$

where the empirical parameters c_1 and c_2 have been determined by Ruijter [55] as 8.0 and 13.0, respectively, for plain weave composites. This expression has been adopted from the damage rule presented in Section 3.2.3.

The stress-strain results obtained in the FE simulation have been compared against the experiment results [50] in Figure 18 below. It can be seen that the experimental curve starts deviating from linear behaviour at a strain of about 0.45%. Obviously, the stress-strain curve for the FE simulation does not show this behaviour because the microstress field is linearly extrapolated from the results obtained in the single unit strain analysis, which does not take into account propagation of damage. In the experiments [50], it was observed by using micrographs that cracks in the transverse yarns were already present at the stress of 187MPa, which explained the non-linear behaviour observed beyond this value. The unit cell failure analysis is in good agreement with these findings. Failure initiation was predicted in the transverse yarns at 168MPa when the Equation (45) was considered, while it was predicted at 96MPa for the most conservative approach. It is important to note that the latter result

corresponds to an applied strain of 0.23%, a typical value for which the first transversal micro-cracks are found in textile composites loaded in tension [56, 57].

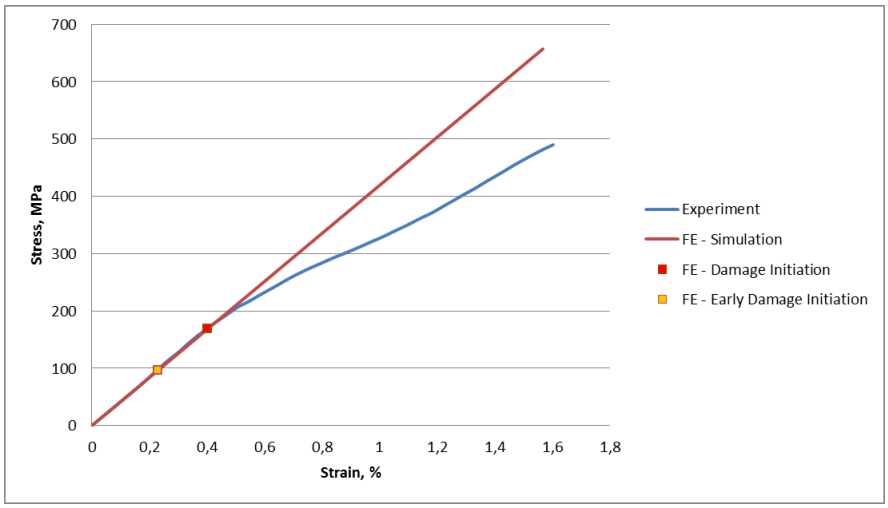

Figure 18. Experimental and FE stress-strain results for the plain woven laminate

Although damage propagation has not been studied, it is interesting to mention that failure in the longitudinal yarn elements was first detected at 1.57% strain, which is very close to the ultimate strain 1.60% found in the in experiments. This proves that final failure of the plain woven composite is governed by the longitudinal yarns, even though the transverse yarns start failing at a much earlier stage. The location of failure initiation for both longitudinal and transverse yarns have been plotted with Matlab as shown in Figure 19 below. It can be noticed that failure initiates at the critical locations observed in Figure 17.

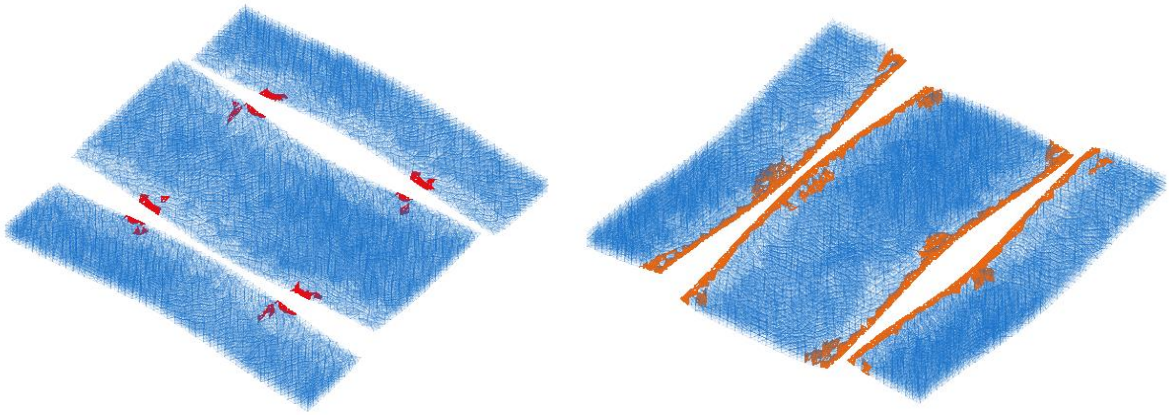

Figure 19. First failed elements in yarns longitudinal (left) and transverse (right) to the loading direction

The same procedure was followed to study the mechanical properties of the twill woven composite. The unit cell homogenization has been carried out by using the material properties listed in Table 7. Periodic BCs in all three directions have been applied since the twill weave laminate consists of 6 isophase layers. The Young's modulus obtained for the RVE-FE simulation is compared against the experimental value [32] in Table 8. The relative error between both results is 7.7%, which is slightly higher than the error obtained for the plain-weave. This might be due to the lower number of layers, which affects the assumption of an infinite periodic medium through the thickness.

Table 7. Material properties of matrix and yarns for twill woven composite [32]

	E_{11}, GPa	$E_{22} = E_{33}$, GPa	$G_{12} = G_{13}$, GPa	G_{23}, GPa	$\nu_{12} = \nu_{13}$	ν_{23}	S_{11}, MPa	S_{22}, MPa	S_{12}, MPa
Epoxy	3.5	3.5	1.29	1.29	0.35	0.35	73	-	-
Yarns (Vf = 0.72)	169.3	9.5	5.1	2.75	0.24	0.37	3498	30	42

Table 8. Homogenized Young's modulus of the twill woven composite

	Experimental value [32]	**FE simulation**	**Error**, %
Young's modulus, GPa	54.1 (1.23)	58.3	7.7

The stress-strain results for both FE simulation and experiment [32] have been plot together in Figure 20 below. It can be observed that the twill composite behaves linearly up to 0.8% strain, while the plain model starts deviating from linear behaviour at 0.45%. However, according to the FE simulation, early failure initiation starts in both cases at very similar strains due to transverse damage in the transverse yarns. Experimental observations [58] have shown that textile composites under tensile loading exhibit similar damage onset scenarios in general, but the cracks can propagate differently depending on the textile architecture. The initiated transverse cracks may stay localized and not propagate immediately through the sample, which explains the different behaviour after damage initiation between plain and twill samples. In fact, a less conservative result is obtained if the initial transverse failure of the yarns is assumed to be given by Equation (45) with parameters $c_1 = 8$ and $c_2 = 24$ [32]. By doing so, it is assumed that the elements do not fail catastrophically when $D_3 > 1$ and the damage onset is then estimated at 0.51% strain.

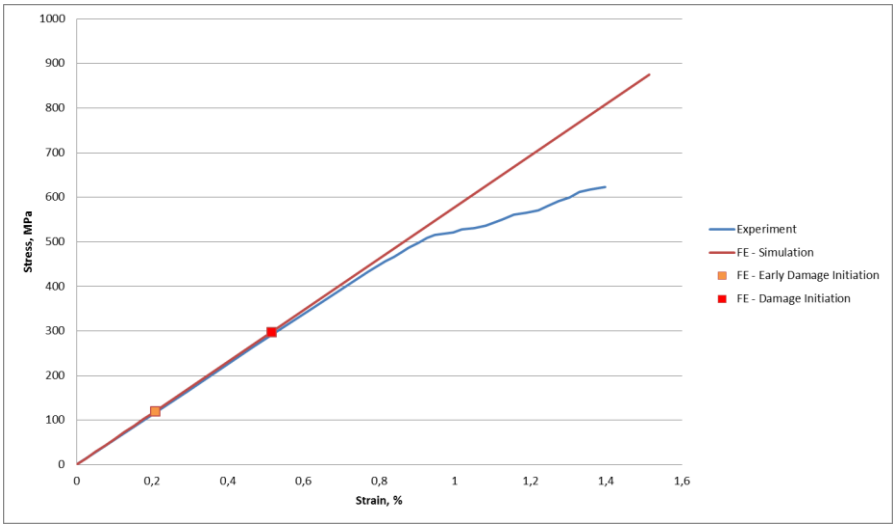

Figure 20. Experimental and FE stress-strain results for the twill woven laminate

Acoustic energy (AE) measurements were performed during the original experimental tests [32] in order to estimate the first damage threshold strain. The result obtained was $\varepsilon_1 = 0.48\%$, which is in good agreement with the last value estimated. However, it was advised to treat the results with caution because a high threshold was used to filter out low energy events. In fact, Lomov and Verpoest [57] performed dedicated AE measurements to predict damage initiation and development in textile composites under tensile loading, where it was found that low energy events start before the first damage threshold strain. Figure 21 below shows a typical AE diagram in which the difference be-

tween the minimum ε_{min} and the first ε_1 damage threshold can be observed. Micrographs taken just after the strain ε_{min} showed the first localised microcracks, while the onset of transversal matrix cracks corresponded to the strain ε_1.

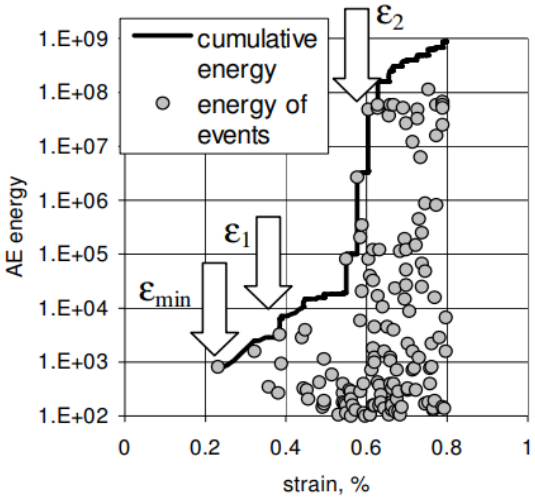

Figure 21. Typical AE diagram (example for a glass/epoxy woven material) at logarithmic scale [57]

The results presented in this section are in reasonable good agreement with the findings made by Ivanov [56], who stated that failure initiation for different textile patterns is remarkably similar when expressed in terms of applied strain. Most of the textile composites loaded in tension show early damage initiation at about 0.15 – 0.35%, while damage initiation appears at approximately 0.6% in cross-ply laminates [59]. The difference is clearly a consequence of the textile geometry. Figure 22 below shows the stress-field and the first damage location for the twill yarns transverse to the loading direction. It can be seen that stress concentrations are present in the yarn edges where the yarns overlap each other, leading to the initiation of transverse cracks.

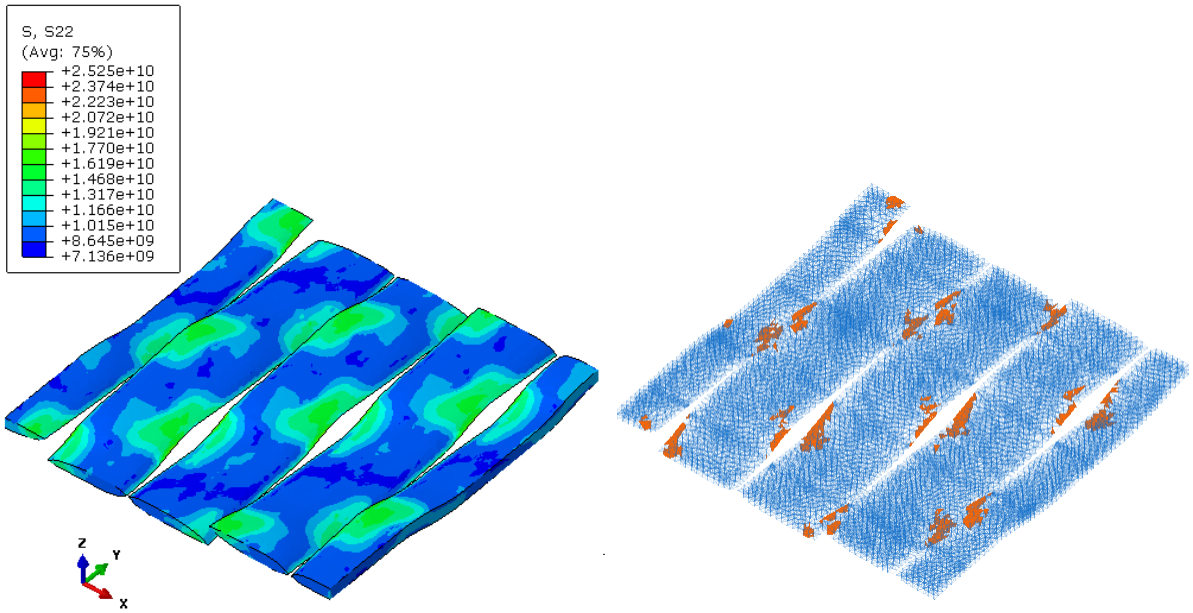

Figure 22. Stress field (Pa) in transverse yarns for a unit strain applied in the x-direction (left) and first damage location (right)

It is concluded that the stiffness and damage onset under tensile loading is well predicted using the methodology presented above. The Young's modulus has been predicted with an error of 4.9% and 7.7% for the plain and twill model, respectively. The error could be reduced by using a multi-layer model of the unit cell instead of a simplified single-layer, but the computational effort would increase dramatically. A realistic model of the RVE geometry is the key for an accurate failure prediction, thus special care should always be taken since stress concentrations will depend on it. The benchmark analysis performed in this section provides confidence to increase the complexly towards multi-axial loading in ultra-thin laminates.

3.3.2 In-plane and out-of-plane loading

The components of the whole ABD matrix have been calculated for the two-ply T300/Hexcel 913 woven composite presented in Section 3.1.3. The samples were produced by using two fabric layers and three film layers of resin. The material properties of the constituents (fiber and matrix) are given in the following Table 9.

Table 9. Fiber and resin elastic properties for the two-ply woven composite [60]

Properties	T300 carbon fiber	HexPly 913 resin
Longitudinal stiffness, E_1 (N/mm^2)	233000	3390
Transverse stiffness, E_2 (N/mm^2)	23100	3390
Shear stiffness, G_{12} (N/mm^2)	8963	1210
Poisson's ratio, ν_{12}	0.2	0.41
Density, ρ (kg/m3)	1760	1230
Areal weight of fabric/film, W (g/m2)	98	30

The first challenge encountered was to estimate the correct fibre volume fraction of the yarns. The unit cell model assumes a perfect rectangular cuboid in which the matrix fills all the volume not occupied by the yarns. However, micrographs images shown in Figure 8 demonstrate that the amount of internal and superficial resin gaps should not be neglected. The original source of the micrographs [60] assumed no voids to calculate the fibre volume fraction of the laminate by using the following expression:

$$V_f^{RVE} = \frac{\rho_m W_f}{\rho_m W_f + \rho_f W_m} \tag{46}$$

from which the overall areal weight of the matrix, W_m, was calculated by using the areal weight of cured samples, W_{comp}, as follows:

$$W_m = W_{comp} - W_f = 280.53 - 98.0 \cdot 2 \; = \; 84.53 \; \mathrm{g/m^2} \tag{47}$$

The overall fiber volume fraction obtained was $V_f^{RVE} = 0.62$, which is unusually high in plain woven composites due to the amount of resin existing in between the yarns. This approach assumes a perfect laminate volume without taking into account manufacturing defects such as surface waviness. These assumptions can lead to unrealistic high fiber volume fractions since the unit cell boundaries are assumed to be perfectly flat. Therefore, an alternative approach is proposed to directly calculate the fibre volume fraction of the yarns without having to use the overall volume of the laminate. First, the mass of a yarn, M^{yarn}, can be calculated by using the following expression:

$$M^{yarn} = \rho^{yarn} \cdot V^{yarn} \tag{48}$$

The volume of a yarn, V^{yarn}, can be obtained from the FE-RVE model and the density of a yarn, ρ^{yarn}, can be calculated by adding up the density of fibres and resin as follows:

$$\rho^{yarn} = \left[V_f \rho_f + \left(1 - V_f\right)\rho_m\right]^{yarn} \tag{49}$$

Also, the following expression can be used to calculate the fiber mass fraction of the yarns, M_f^{yarn}:

$$M_f^{yarn} = \frac{\left[V_f \rho_f\right]^{yarn}}{\rho^{yarn}} \tag{50}$$

The expressions above depend on the unknown fibre volume fraction of the yarns, V_f^{yarn}. However, the areal weight of the fabric, W_f, is known from the manufacturing datasheets and the area of the RVE, A^{RVE}, can be obtained from the micrographs. Therefore, the mass of a yarn can alternatively be calculated as follows:

$$M^{yarn} = \frac{M^{fibre-bundle}}{M_f^{yarn}} \tag{51}$$

where $M^{fibre-bundle}$ is the mass of the bundle of fibres and can be deduced from the number of yarns in the RVE, n_{yarns}, as follows:

$$M^{fibre-bundle} = \frac{1}{n_{yarns}} W_f A^{RVE} \tag{52}$$

The volume of a yarn was calculated from the unit cell model by using Abaqus and the result obtained was $V^{yarn} = 0.125\ \mathrm{mm}^3$. Finally, the fibre volume fraction of the yarns can be obtained by setting the Equation (48) and (52) equal to each other. The result obtained was $V_f^{yarn} = 0.75$, which is in agreement with the typical dense fibre packing values observed inside the yarns of woven composites [61]. The result is also within the theoretical limits of fiber packing arrangement, which are illustrated in Figure 23. The maximum V_f is equal to 0.785 for the square configuration, and 0.907 for the hexagonal one.

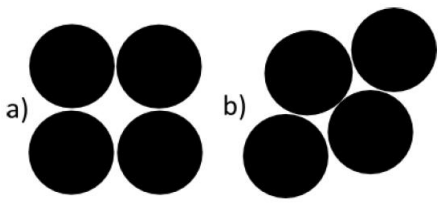

Figure 23. Fiber packing arrangement; (a) square and (b) hexagonal [62]

The overall fiber volume fraction of the laminate can now be calculated by using the following expression:

$$V_f^{RVE} = \frac{n_{yarns} \cdot V_f^{yarn} \cdot V^{yarn}}{V^{RVE}} \tag{53}$$

where the volume of the RVE is found from the FE-RVE model as 1.56 mm^3. The overall fiber volume fraction obtained was finally calculated to be $V_f^{RVE} = 0.48$, which agrees very well with typical plain weave composite experimental values [63]. As a conclusion, the approach presented above ensures to obtain an accurate fibre volume fraction of the yarns by directly using the geometry of the impregnated yarn, which is derived from the micrographs, and the mass of the bundle of fibres, which is given by the manufacturing data sheets. Furthermore, this approach allows to estimate the fibre volume content of hybrid multilayer composites, as it will be shown in Chapter 4.

Once the fibre volume fraction of the yarns has been estimated, the homogenized elastic properties can be calculated by using the analytical micromechanical models described in Section 2.3.1. The material properties of the constituents have been used as given in Table 9, and the following results have been obtained:

Table 10. Homogenized elastic properties of the T300/913 yarns for $V_f = 0.75$

Material Properties	Value
Longitudinal stiffness, E_1 (N/mm^2)	175597
Transverse stiffness, $E_2 = E_3$ (N/mm^2)	12985
Shear stiffness, $G_{12} = G_{13}$ (N/mm^2)	4439
Transverse shear stiffness, G_{23} (N/mm^2)	4595
Poisson's ratio, $\nu_{12} = \nu_{13}$	0.253
Poisson's ratio, ν_{23}	0.413

The values listed in Table 10 above have been used to characterize the yarns as homogenized continua in the unit cell model. The constitutive [A], [B] and [D] matrices have been calculated for the three layer shift configurations defined in Section 3.1.3. The six macroscopic unit deformation have been applied with the corresponding boundary conditions shown in Table 4. The results for both tensile and bending loading have been compared against experimental data [60] in Table 11 by considering the following relations:

$$\varepsilon_x = a_{11} N_x \tag{54}$$

$$M_x = D_{11} \kappa_x \tag{55}$$

Table 11. Homogenized material properties of the two-ply woven composite

Unit cell model	$\mathbf{1/a_{11}}$ [N/mm]	$\boldsymbol{\nu_{12}}$ [-]	$\mathbf{D_{11}}$ [N·mm]
In-phase	12389	0.119	45.5
Out-of-phase	13212	0.043	40.8
$\pi/4$ phase	12769	0.095	42.9
Experiments [60]	12833 (12,070 – 13,220)	0.11 (0.05 – 0.14)	37.84 (30.58 – 45.81)

The original source of the experiment noted a significant variation of certain results but it did not argue the possible reasons. The minimum and maximum value have been shown in Table 11 above in order to highlight the difference. As it can be seen, the results for the three layer shift configurations are within the range found in the experiments. The models with the layers in-phase and π/4 out-of-phase are the most representative for the sample average. It is interesting to note that the layer shift

observed in Figure 8 is in between these two configurations, which might be the reason for this similarity. However, the strong variation observed in the experimental bending stiffness is not explained by the layer shift. It is very likely that samples had slightly different thickness as a consequence of the manufacturing process, which would affect the bending properties significantly. However, the thickness of each sample was not measured during the experiments, thus it is not possible to make a proper comparison.

It has been shown that the stiffness results for the model with the layers π/4 out-of-phase are in between the two other two extreme configurations. Hence, this model has been chosen in order to study failure initiation under in-plane and out-of-plane loading by using the aforementioned procedures. The results of maximum principal stresses under each independent macroscopic unit deformation are shown in Figure 24 below. It can be observed that the critical locations are always close to the yarn edges where the yarns overlap each other. Furthermore, it is particularly interesting to note that the top and bottom layer present similar stress distribution patterns for each load case except $\kappa_x = 1$, where the longitudinal yarns are loaded in tension in the top and compression in the bottom. The entries of the constitutive ABD matrix were found to be as follows:

$$ABD = \begin{bmatrix} 12885 & 1220 & 0 & 0 & 0 & 0 \\ 1220 & 12885 & 0 & 0 & 0 & 0 \\ 0 & 0 & 707 & 0 & 0 & 0 \\ 0 & 0 & 0 & 42.9 & 5.4 & 0 \\ 0 & 0 & 0 & 5.4 & 42.9 & 0 \\ 0 & 0 & 0 & 0 & 0 & 2.5 \end{bmatrix} \tag{56}$$

where the units are in N and mm.

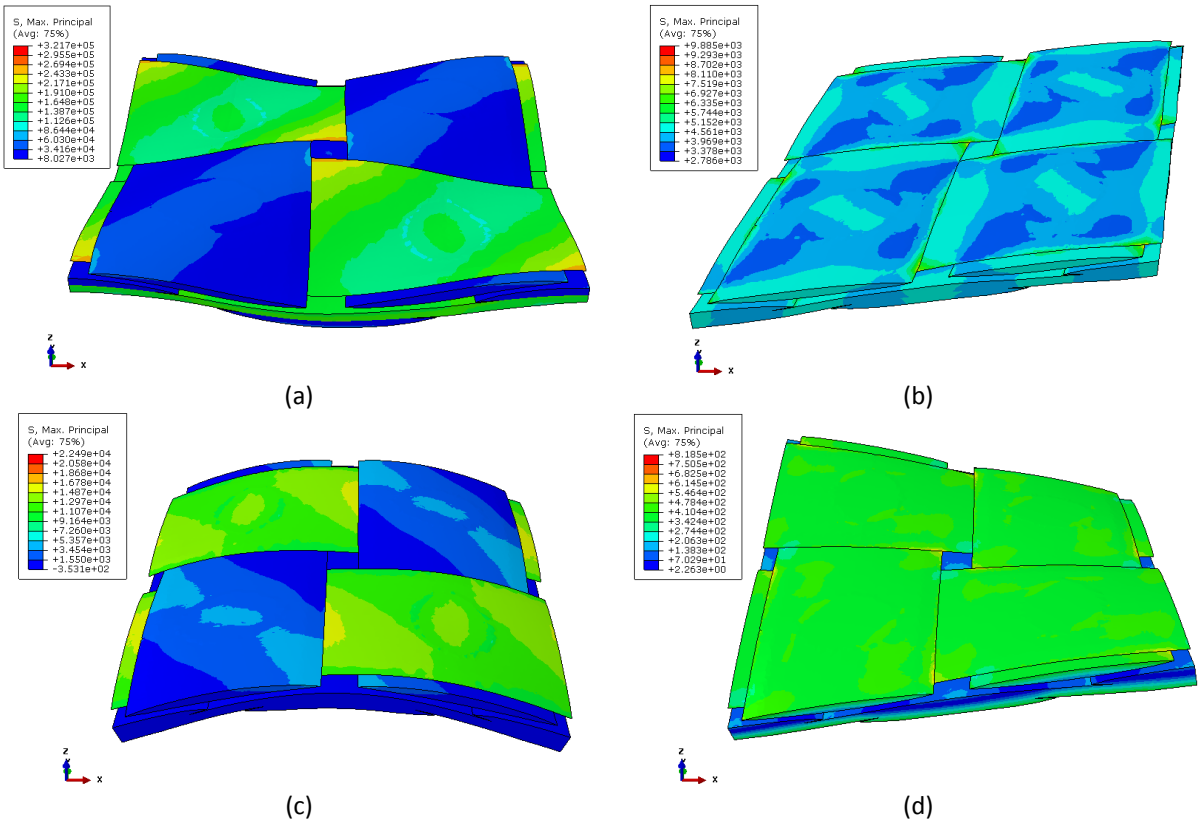

Figure 24. Stress field (MPa) for the two-ply weave composite under (a) $\varepsilon_x = 1$, (b) $\gamma_{xy} = 1$, (c) $\kappa_x = 1$, and (d) $\kappa_{xy} = 1$

It should be noted that the prediction of failure initiation under shear loading required special considerations. The shear response was first calculated by using the following strength material properties:

Table 12. Yarn and matrix strength material properties for the two-ply woven composite [60]

Material Properties	T300/913 UD	HexPly 913 resin
Longitudinal tensile strength, σ_{1t}^{u} (N/mm^2)	2005	65.5
Longitudinal compressive strength, σ_{1c}^{u} (N/mm^2)	1355	-
Transverse tensile strength, σ_{2t}^{u} (N/mm^2)	68	-
Transverse compressive strength, σ_{2c}^{u} (N/mm^2)	198	-
Shear strength, σ_{s}^{u} (N/mm^2)	150	-

The yarns were assumed to have the same strength properties of a unidirectional composite. Failure was checked element-by-element while the shear loading was gradually increased. First-element failure was found due to shear cracking in the yarns at the load $N_{xy} = 17.5\ \mathrm{N/mm}$. However, the experimental stress-strain curve [60] showed deviation from the linear behavior at a much lower value. Therefore, a different approach was attempted to predict the initiation of failure. The unit cell model was rotated 45 degrees in order to simulate a [±45] tensile test and thus evaluate the shear response. It is important to mention that the size of the RVE had to be increased by $\sqrt{2}$ in order to keep the periodic geometry, as shown in Figure 25 below. Otherwise, the periodic BCs are not applicable.

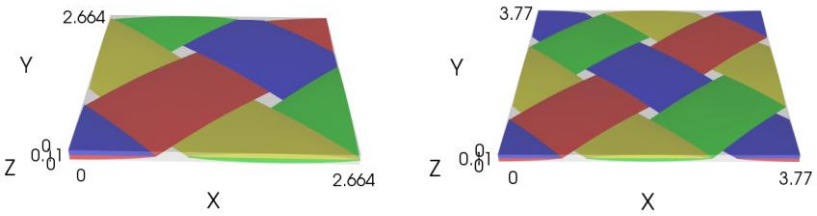

Figure 25. Rotation of the unit cell

The homogenization and the failure analysis of the rotated unit cell was performed as before. The following expressions were used to determine the shear resultant and strain:

$$N_{xy} = \frac{N_x}{2} \tag{57}$$

$$\gamma_{xy} = \varepsilon_x - \varepsilon_y \tag{58}$$

First-element failure was found at the same load and strain. A possible error in the methodology was ruled out since the tensile loading has been already validated. Thus, the assumed strength parameters of the impregnated yarns were questioned. Ito and Chou [50] found that the critical shear strength σ_s^u depends on the location in the yarn, with the centre line having higher values. To take this into account, they recommended to apply the shear strength of the fabric composite as the critical shear strength value for the yarns. Mallikarachchi [60] estimated the pure shear strength of the

two-ply weave laminate as $\sigma_s^u = 80.59\ \mathrm{N/mm^2}$. The failure analysis under shear loading was then conducted by using this value and the following result was obtained.

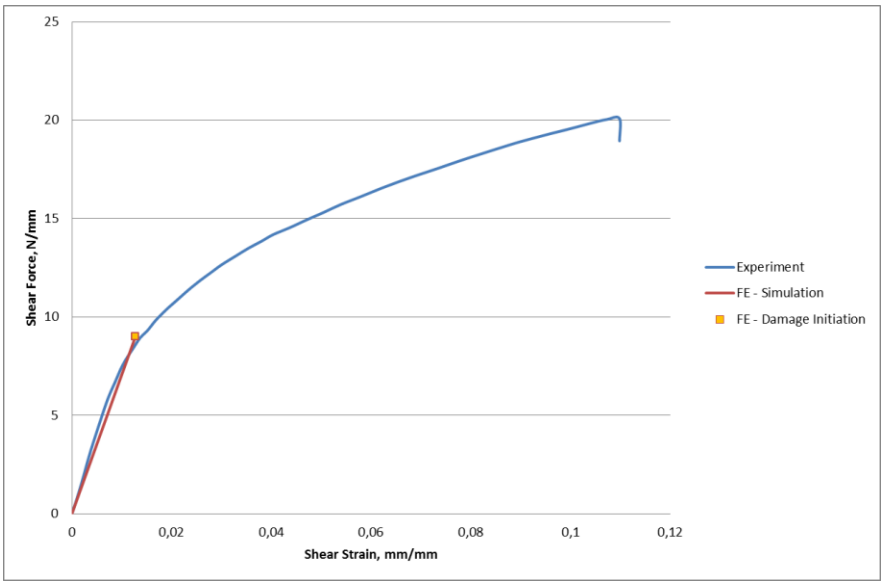

Figure 26. Experimental and FE shear response for the two-ply weave composite

First-element failure was found due to shear cracking in the yarns at the load $N_{xy} = 9.0\ \mathrm{N/mm}$ and the strain $\gamma_{xy} = 0.013$, which agrees reasonably well with the initial deviation from linear behaviour observed in the experimental curve. Furthermore, the damage mode coincides with the experimental studies reported by Lisle et al. [64], where they observed matrix microcracks in the yarns as the damage initiation mechanism. After this validation, first-element failure was calculated for pure tension, compression, shear, bending and torsion loading by assuming that the yarns have the strength properties of the unidirectional composite and the critical shear strength of the fabric composite. The modified maximum stress criteria has been compared against Tsai-Wu criteria to predict failure of the yarns. The results obtained are shown in Table 13 below.

Table 13. Uniaxial failure strengths for the two-ply woven composite

Load	**Ultimate Strength** [60]	**Failure Initiation Load**	
		Max. Stress	**Tsai-Wu**
Tension, N/mm	139.47	49	49
Compression, N/mm	63.42	66	60
Shear, N/mm	17.73	9.0	9.5
Bending, Nmm/mm	3.04	1.6	1.6
Torsion, Nmm/mm	0.92	0.45	0.50

As it was expected, it can be seen that failure initiation is predicted at much lower values than the experimental ultimate strength, except for compression loading. The reason is that compression loading causes first failure in the load-aligned yarns, which leads to catastrophic failure. Therefore, it is safe to assume that the entire material fails when failure of the longitudinal yarns is detected [65]. Failure initiation was found in the transverse yarns for tension and bending. Specifically, bending loading lead to failure in the transverse yarns of the top layer due to tensile stresses. Finally, shear failure in both weft and warp were found in shear and torsion loading. It can be concluded that the

modified maximum stress criteria and Tsai-Wu give very similar results. However, the modified maximum stress criteria is preferred since it has allowed to detect the damage mode, which has been extremely useful to understand the mechanisms of failure initiation.

3.4 Conclusions

The multi-scale approach presented in this chapter has demonstrated to be a powerful method to predict the elastic properties of woven composites, as well as the failure initiation under in-plane and bending loads. However, it presents some challenges and limitations that should be pointed out. First of all, the modelling and discretization of the RVE is a very time-consuming task. The software TexGen and its python interface have been found very useful to generate almost any textile geometry, but the process can become very tedious if a realistic unit cell model is wanted. Despite the solutions proposed, the mesh generation can require some trial and error until a good quality mesh is obtained. Regarding the methodology itself, the major limitation is the linear assumption to extrapolate the results obtained in the single unit strain analyses. As has been shown, this assumption allows to estimate the initiation of failure, but limits the possibility of studying damage propagation. A totally different approach would be necessary to study the non-linear material behaviour after failure initiation.

The estimation of failure initiation using the unit cell approach might be considered conservative if the mechanisms of failure initiation are not taken into account. It has been observed that the first micro-cracks initiate at relatively low strain level due to the stress concentrations caused by the interlacing warp and weft yarns. Although these micro-cracks do not immediately propagate, they realistically represent the initial damage of the composite. These findings have been contrasted with those from acoustic energy measurements, which detect low energy events at similar strain levels. The unit cell approach allows to predict the location of failure, so the results should be interpreted depending on the damage mode detected.

It is important to note that an accurate prediction of the overall mechanical behaviour would not have been possible without a correct estimation of the homogenized mechanical properties of the yarns. The entire micromechanical model depends on the fibre volume fraction of the yarns, so special attention has been paid on the methodology to estimate its value. The proposed approach will be used in the following section to estimate the mechanical properties of hybrid laminates composed of woven and unidirectional layers.

Chapter 4 Hybrid Woven/UD Laminates

This chapter presents a case study of hybrid laminates composed of two woven layers with a ply of UD fibres between them. The tape-springs have been produced using this laminate stacking sequence in order to obtain improved mechanical properties. Two different configurations have been analyzed, the first one using plain weave layers, and the second one using twill weaves. First of all, the fibres' architecture has been measured from micrographs. The data obtained have been used to analyze each layer separately. Secondly, the woven layers have been discretized in the mesoscale to estimate the fibre volume fraction and the yarn properties, which are not known a priori. Then, the material properties of the lamina have been homogenized using the aforementioned FE-RVE approach. Subsequently, the material properties of the UD layer have been estimated using an analytical approach that considers the influence of ply waviness on the stiffness. The overall laminate properties have been finally calculated using the Classical Laminate Theory. The results obtained here will be used in Chapter 5 to predict the macroscopic failure behaviour of the tape-springs.

4.1 Micrograph Measurements

The laminates for the micrographs were directly cut from the tape-spring samples as shown in Figure 27. The tape-spring were previously tested until failure, thus the laminate samples were taken as far as possible from the damaged area. The UD and the woven layers are oriented in the 0° and 45° direction, respectively. Therefore, the samples were cut in both directions in order to measure the weave length and the cross-sectional area of the yarns, as well as to analyze the cross-section of the UD layer.

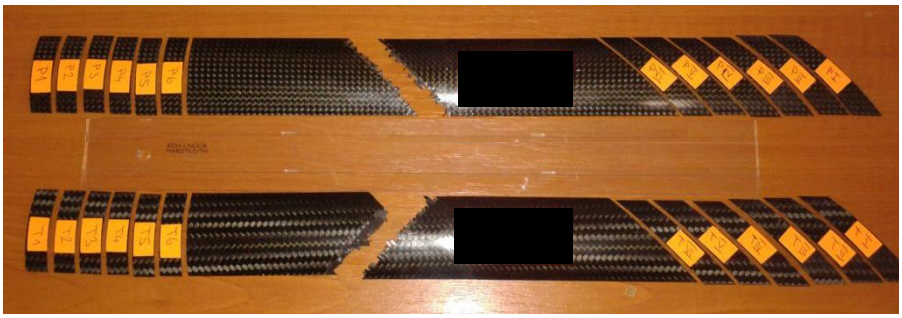

Figure 27. Samples preparation

The samples were cut with dimensions N × M and then polished in order to avoid scratches in the surface. The micrographs were obtained with the help of the *Laboratoire physico-chimique* at Thales Alenia Space by using the microscope with ×N1 and ×N2 magnification. An example of the images taken for the twill weave and plain weave samples is shown, respectively, in Figure 28 and Figure 29 below.

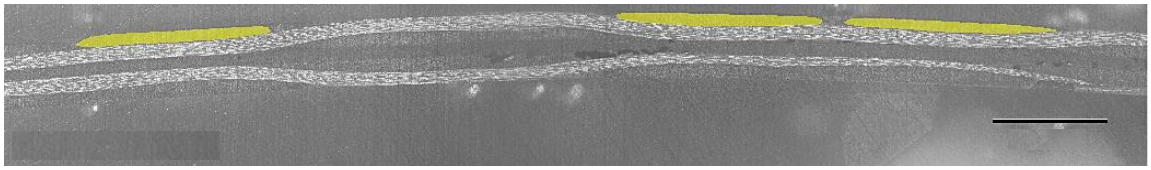

Figure 28. Micrograph of Twill/UD/Twill hybrid laminate

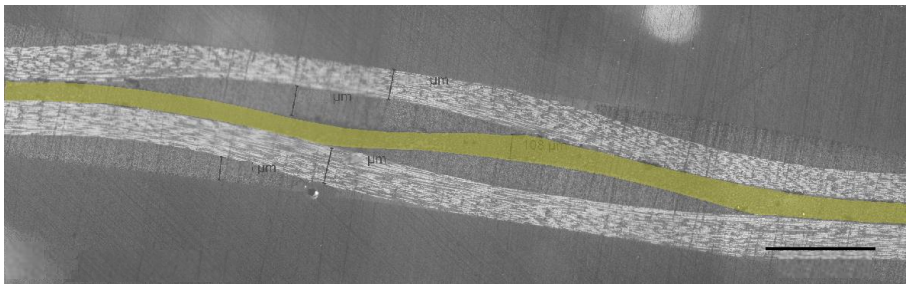

Figure 29. Micrograph of Plain/UD/Plain hybrid laminate

The micrographs images were imported into Matlab and the geometric properties listed in Table 14 were measured by using the Image Segmenter Toolbox. The resolution of the micrographs was not high enough to apply a threshold that automatically select the image regions having similar gray levels. Thus, the edges of the yarns and the UD were defined by using a continuous polygon drawn. The data points were used to calculate the geometric dimensions needed to create the unit cell model.

Table 14. Geometric properties of the plain and twill weave layers

	Plain weave layer	**Twill weave layer**
RVE weave length, mm	-	-
Maximum tow thickness, mm	-	-
Tow cross-sectional area, mm^2	-	-

Micrographs showed that significant ply waviness exists in the UD layer between the two plain woven plies. The undulation amplitude can be observed in Figure 29, where the UD layer has been highlighted in yellow. However, it is noted that there is no ply waviness in the UD layer between the two twill woven plies. This difference may be attributed to the layer shift rather than the different textile architecture. On the one hand, the top and bottom plain weave layers are approximately π/4 out-of-phase, thus the UD layers tends to follow the weaving pattern. On the other hand, the twill samples show a perfect out-of-phase shift between the woven layers, which allows to keep the UD layer in a flat configuration. The weaving parameters shown in Table 15 have been obtained from the micrographs in order to study the effect of the UD waviness on the mechanical properties as it is further detailed in Section 4.2.2. It is important to note that the image shown in Figure 29 has been taken from a sample cut in 45°, while the UD layer is oriented in the 0° direction. Therefore, Equation (59) below has been used to estimate the weave length of the UD layer in the fibre direction:

$$UD\ weave\ length = \sqrt{2} \cdot \frac{RVE\ weave\ length}{2} \tag{59}$$

Table 15. Weaving parameters of the UD layer

	Plain weave laminate	**Twill weave laminate**
UD ply thickness, mm	-	-

UD peak-to-peak thickness, mm	-	-
UD weave length, mm	-	-

The geometric parameters presented above will be used in the following Section 4.2.1 to create the unit cell models of the woven layers by using TexGen. Furthermore, the findings regarding the UD waviness will be studied in Section 4.2.2 to quantify the influence of manufacturing defects on the overall stiffness of ultra-thin hybrid laminates.

4.2 Estimating Elastic Material Properties

4.2.1 Woven layer

The first parameter required to estimate the elastic properties of the woven layer is the fibre volume content of the yarns. This parameter cannot be calculated from the areal weight of the laminate since the woven and the unidirectional layers are composed of different constituent materials (fibre and matrix) with different densities. The alternative method proposed in Section 3.3.2 was therefore used for this purpose. First, the unit cell model of the woven layers was created using TexGen in order to calculate the volume of the yarns. The geometric parameters from the micrograph measurements were used to model both plain and twill configurations as follows:

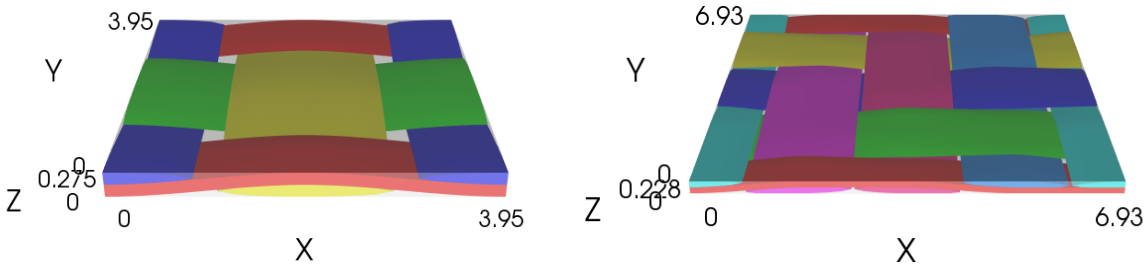

Figure 30. Plain and twill layer models for the hybrid laminate

The volume of one yarn was measured by using Abaqus, obtaining 0.665 mm^3 for the plain model and 0.947 mm^3 for the twill model. The density of the fibres and the matrix, as well as the areal weight of the fabric are detailed in the Appendix I. The fibre volume fraction of the yarns was obtained by setting the Equation (48) and (52) equal to each other, obtaining $V_f^{yarn} = 0.65$ and $V_f^{yarn} = 0.69$ for the plain and twill configurations, respectively. Then, the transversely isotropic material patermers of the yarns were estimated using the micromechanical analytical models described in Section 2.3.1. The following results were obtained:

Table 16. Homogenized elastic properties of the yarns for the plain and twill configurations

Material Properties	Plain weave	Twill weave
Longitudinal stiffness, E_1 (N/mm2)	-	-
Transverse stiffness, $E_2 = E_3$ (N/mm^2)	-	-
Shear stiffness, $G_{12} = G_{13}$ (N/mm^2)	-	-
Transverse shear stiffness, G_{23} (N/mm^2)	-	-
Poisson's ratio, $\nu_{12} = \nu_{13}$	-	-
Poisson's ratio, ν_{23}	-	-

The homogenization of the unit cell models was conducted by applying the periodic boundary conditions described in Table 4. The procedure described in Section 3.2 was followed and the following stiffness matrices were obtained:

$$ABD^{plain} = \begin{bmatrix} - & - & 0 & 0 & 0 & 0 \\ - & - & 0 & 0 & 0 & 0 \\ 0 & 0 & - & 0 & 0 & 0 \\ 0 & 0 & 0 & - & - & 0 \\ 0 & 0 & 0 & - & - & 0 \\ 0 & 0 & 0 & 0 & 0 & - \end{bmatrix} \tag{60}$$

$$ABD^{twill} = \begin{bmatrix} - & - & 0 & 0 & 0 & 0 \\ - & - & 0 & 0 & 0 & 0 \\ 0 & 0 & - & 0 & 0 & 0 \\ 0 & 0 & 0 & - & - & 0 \\ 0 & 0 & 0 & - & - & 0 \\ 0 & 0 & 0 & 0 & 0 & - \end{bmatrix} \tag{61}$$

where the units are in N and mm.

4.2.2 UD layer

The goal of this subsection is to investigate the stiffness reduction due to ply waviness of the unidirectional layer. As it has been previously shown in the micrographs images, the UD fibres may conform to the adjacent plain woven plies, which might not be negligible. Bogetti et al. [66] developed an analytical model that estimates the stiffness reduction by assuming ply waviness in only one direction. The wavy ply geometry and the corresponding unit cell are schematically depicted in Figure 31 below.

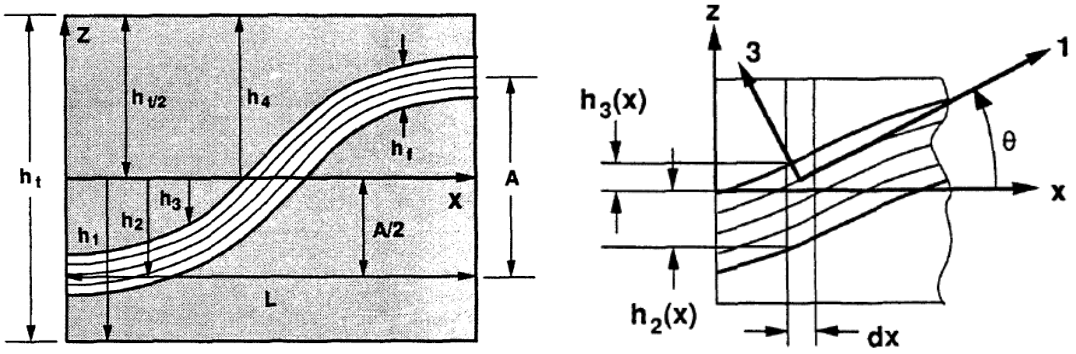

Figure 31. UD ply waviness: Unit cell [66]

The wavy ply configuration is idealized as a sine wave, where A is the amplitude of the undulation and L is the half-wavelength. The representative unit cell can be mathematically defined as a function of x. Specifically, the distances along the half-sine are written by Bogetti et al. [66] as follows:

$$h_2(x) = -\frac{A}{2} - \frac{h_f}{2} + \left[1 + \sin\left(\frac{\pi}{L}\left(x - \frac{L}{2}\right)\right)\right]\frac{A}{2} \tag{62}$$

$$h_3(x) = -\frac{A}{2} + \frac{h_f}{2} + \left[1 + \sin\left(\frac{\pi}{L}\left(x - \frac{L}{2}\right)\right)\right]\frac{A}{2} \tag{63}$$

The expression above can be used to define the local out-of-plane undulation angle as follows:

$$\theta(x) = \tan^{-1}\left[\frac{d\big(h_2(x)\big)}{dx}\right] = \tan^{-1}\left[\frac{d\big(h_3(x)\big)}{dx}\right] \tag{64}$$

The approach consists in applying the classical laminate theory to each segment of width dx in which the unit cell is divided. The effective response is obtained by averaging the compliances assuming constant in-plane stress within each discrete segment. First, the ABD matrices for each segment are calculated by using the $h_i(x)$ values given above. For this, the stiffness matrix Q_{ij} must take into account the out-of-plane orientation, thus the effective engineering properties are given as a function of the undulation angle as follows:

$$E_x(\theta) = \left[\frac{l_\theta^4}{E_1} + \left(\frac{1}{G_{13}} - 2\frac{\nu_{13}}{E_1}\right) l_\theta^2 m_\theta^2 + \frac{m_\theta^4}{E_3}\right]^{-1} \tag{65}$$

$$E_y(\theta) = E_2 \tag{66}$$

$$\nu_{xy}(\theta) = E_x(\theta)\left[\frac{\nu_{12} l_\theta^2}{E_1} + \frac{\nu_{32} m_\theta^2}{E_3}\right] \tag{67}$$

$$G_{xy}(\theta) = \left[\frac{m_\theta^2}{G_{23}} + \frac{l_\theta^2}{G_{12}}\right]^{-1} \tag{68}$$

where

$$l_\theta = \cos\theta \tag{69}$$

$$m_\theta = \sin\theta \tag{70}$$

The effective [abd] matrices for each segment can be directly computed through inversion of the [ABD] matrices. However, it should be noted that local warping, i.e. local out-of-plane deformation, is allowed in the model presented above. Ishikawa and Chou [67] stated that local warping may be constrained by the adjacent layers in a multilayer composite. Both behaviors are limiting conditions, a warping suppressed condition may be more realistic for laminates of appreciable thickness. The in-plane compliance matrix a_{ij} can be rewritten with local warping constrained as follows:

$$a_{ij}^* = \left[a_{ij} - b_{ij} d_{ij}^{-1} b_{ij}\right] \tag{71}$$

Then, the average in-plane compliance for both limiting conditions can be obtained by the following integration:

$$a_{ij}^{**} = \frac{1}{L}\int_0^L a_{ij}(x)\,dx \quad \text{or} \quad a_{ij}^{**} = \frac{1}{L}\int_0^L a_{ij}^*(x)\,dx \tag{72}$$

Finally, the average mechanical properties of the wavy ply are calculated by using the compliance coefficients above and the Equations (32).

It is important to note that the model takes into account ply waviness in only one direction. However, the woven ply architecture of the adjacent plies will deform the unidirectional ply along the whole

x-y plane. The goal is to quantify the influence of undulation on the stiffness reduction in the load direction because significant variations have been noticed on different tape-spring samples as it will be further explained in Section 5.3. Therefore, it is acceptable to assume ply waviness in only the fibre direction since the undulation on the transversal direction will barely have an effect.

The mechanical properties of the UD composite prepreg are given in Appendix I. The reduction of the original properties have been estimated using the approach described above and the geometric weaving parameters listed in Table 15. The graph in Figure 32 shows the effect of the undulation amplitude on the Young's modulus E_x for both local warping limiting cases. The results indicate that there is a significant stiffness reduction for the undulation amplitude measured from the micro-graphs. As it was expected, stiffness reduction is not as severe when local warping is constrained (~25%) than when local warping is allowed (~40%). Although predictions based on local warping allowed may be too conservative for a thick laminate, they may match better for the ultra-thin laminates used in the tape-springs.

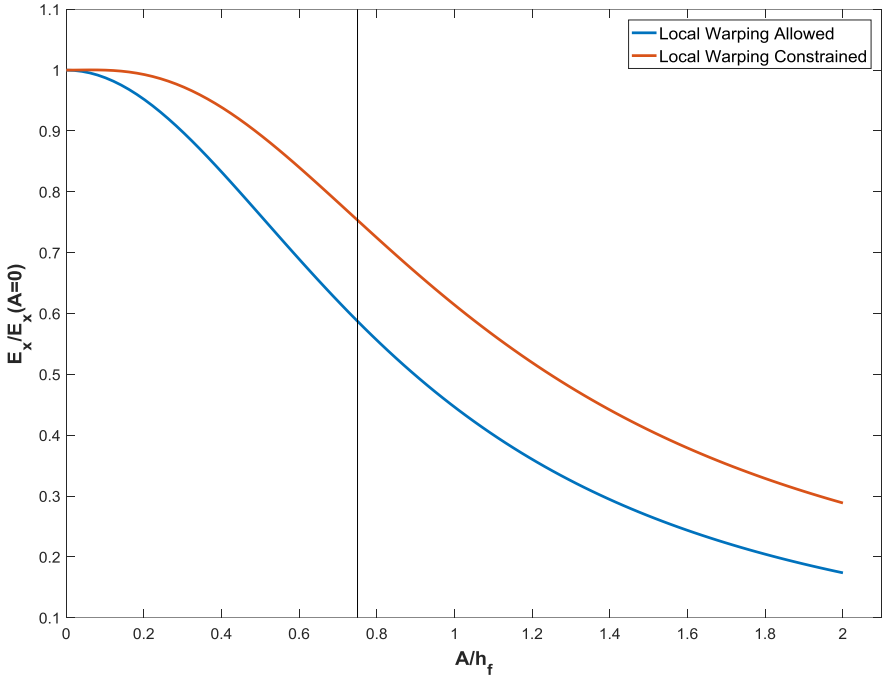

Figure 32. Influence of undulation amplitude on E_x

The results obtained above will explain the significant difference in mechanical properties between tape-springs made out of plain and twill weave patterns, as it will be further detailed in Section 5.3. The manufacturing process strongly influences the relative position between the external woven layers, which directly affects the waviness of the UD layer in the middle. From the graph shown in Figure 32 above, it can be stated that the ratio A/hf should be lower than ~0.3 in order to avoid a stiffness reduction larger than 10%. For this, the shift between the exterior woven layers should be avoided in order to reduce the undulation amplitude of the UD layer.

4.2.3 Overall Laminate

The constitutive [ABD] matrices for the multi-layer composite will be required for the macroscopic failure analysis of the tape-spring, as further detailed in Section 5.2.2. The expression for the overall stiffness can be written as follows:

$$A_{ij}^{ML} = \sum A_{ij}^{SL} \tag{73}$$

$$D_{ij}^{ML} = \sum \left(D_{ij}^{SL} + A_{ij}^{SL} h^2 \right) \tag{74}$$

where the superscripts SL and ML represent, respectively, single-layer or multi-layer properties, and h is the distance from the bending axis to the centre of a layer. Note that the coupling [B] matrix is not accounted since laminates with zero [B] terms have to be used for the tape-spring application.

It is important to note that the ABD matrices for each single layer should be defined in the same global direction in order to apply the Equations (73) and (74) above. The material direction of the woven layers have been chosen for simplicity. The goal is simply to reduce as much as possible the number of coordinate transformations in the macroscopic failure analysis. The results for each laminate configuration are shown in Appendix I.

4.3 Failure Parameters

The strength of the yarns need to be known in order perform the failure analysis of the woven and twill models. Except the transverse tensile strength, which strongly depends on the matrix, the yarns can be assumed to have similar strength properties in composites with the same types of fibres and volume fractions. Therefore, the strength of the yarns were taken from those given in Section 3.1.3 for the two-ply woven composite, excluding the transverse tensile strength, which has been estimated based upon the ratio of the different resin strengths [50]. Note that this indicates that the strength of the yarns in the transverse direction can be greatly improved by using high-strength resins. The values for yarns and matrix are listed in Table 17.

Table 17. Yarn and matrix strength material properties for the hybrid woven laminates

Material Properties	Yarns	Resin
Longitudinal tensile strength, σ_{1t}^{u} (N/mm^2)	-	-
Longitudinal compressive strength, σ_{1c}^{u} (N/mm^2)	-	-
Transverse tensile strength, σ_{2t}^{u} (N/mm^2)	-	-
Transverse compressive strength, σ_{2c}^{u} (N/mm^2)	-	-
Shear strength, σ_{s}^{u} (N/mm^2)	-	-

As explained in Section 2.4, the failure criterion proposed by Mallikarachchi and Pellegrino [44] can be expressed in terms of six different coefficients, which can be written as follows:

$$D_1 = \frac{1}{F_{1t}} - \frac{1}{F_{1c}} \qquad C_{44} = \frac{1}{F_4^2}$$
$$C_{11} = \frac{1}{F_{1t}F_{1c}} \qquad C_{66} = \frac{1}{F_6^2} \tag{75}$$

$$C_{33} = \frac{1}{F_3^2} \qquad C_{12} = -\frac{C_{11}}{2}$$

where,

- F_{1t} is the tension failure strength,
- F_{1c} is the compression failure strength,
- F_3 is the shear failure strength,
- F_4 is the bending failure strength,
- F_6 is the twisting failure strength.

As has been demonstrated in previous sections, the five uniaxial failure strengths can be calculated using the micromechanical unit cell approach. However, it should be noted that Mallikarachchi and Pellegrino [44] obtained these values from failure strength experiments, which indicate the ultimate failure loads. The unit cell failure analysis give the values corresponding to failure initiation. Therefore, the failure predictions will be considerably more conservative, but they will realistically represent the initial damage. Table 18 shows the failure strength results obtained for both plain and twill woven models. The two definitions of initial transverse and shear failure of the yarns, presented in Section 3.3.1, have been considered.

Table 18. Uniaxial failure strengths for the plain and twill woven laminas

Strength	Plain woven	Twill woven
$F_{1t} = F_{2t}$, N/mm	-	-
$F_{1c} = F_{2c}$, N/mm	-	-
F_3, N/mm	-	-
$F_4 = F_5$, Nmm/mm	-	-
F_6, Nmm/mm	-	-

(*) Early failure initiation

It is important to note that failure envelopes for the woven composites could be generated by gradually increasing a selected force or moment resultant. This approach on its own will not be readily applicable to predict failure in multiaxial loading conditions at the macroscopic level since the various force and moment resultant spaces will be many and quite different in nature, which is why the phenomenological failure criteria proposed by Mallikarachchi and Pellegrino [44] will be used. However, the potential of the micromechanics method should not be overlooked, as it could be used to replace complex experimental tests. As an example, the micromechanics approach has been used to study failure under biaxial bending and confirm the hypothesis that the value of M_x at failure is practically independent of M_y in woven composites [46]. As a comparison, the biaxial N_x – N_y force envelope has also been plotted to show that the interaction between these loads is effectively quadratic. Figure 33 below shows the result obtained for the plain woven lamina studied in this section.

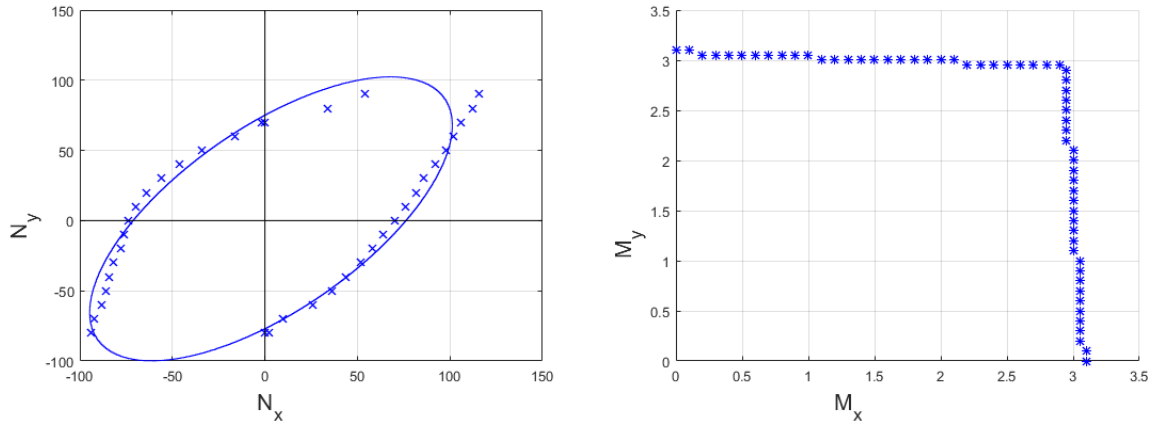

Figure 33. Failure envelopes for biaxial loads (left) and moments (right)

4.4 Conclusions

The complexity of the laminate has been increased in this section by combining both woven and UD layers. The homogenization of the entire composite has been carried out layer by layer. On the one hand, the material properties of the impregnated woven layers have been estimated by using the geometric properties measured from the micrographs and the unit cell approach described in the previous Chapter 3. For this, the fiber volume content has been estimated by just looking at the geometric and material constituents of the yarns. The woven and UD layers are composed of different types of fibre and resin, thus traditional approaches to measure the fibre volume content cannot be used.

On the other hand, the micrographs have shown severe ply waviness of the unidirectional layer. This manufacturing defect has been attributed to the layer shift between the woven layers. As shown in Section 3.3.2, layer shift do not have a significant impact in ultra-thin woven composites. However, this is completely different for hybrid composites since the UD layer can be affected. An analytical approach based on the classical laminate theory has been used to estimate the effect of the undulation amplitude on the stiffness reduction. The results show that its effect cannot be neglected as has been done so far. The fact that the twill woven layers are in perfect out-of-phase, contrary to the plain woven layers, might be just a coincidence. Therefore, more attention should be given to control the layer shift during the manufacturing of the tape-springs.

Finally, the failure parameters required to perform the failure analysis of the entire tape-springs have been calculated. An important finding in this regard is that the strength of the yarns in the transverse direction can be greatly improved by using high-strength resins. As shown in Chapter 3, early failure initiation under tensile and bending loading is caused due to transverse damage in the transverse yarns, thus the initiation of the first micro-cracks could be significantly affected by just changing the type of resin.

Chapter 5 Analysis of Tape-springs

The aim of this chapter is to estimate failure initiation of tape-springs under multi-axial loading conditions. The mechanical properties calculated on the mesoscale will now be used to analyze the macroscopic behaviour. A series of tape-springs have been produced and tested by a contractor. The details of the experimental set-up will be first introduced in order to reproduce the test using the finite element method. The simulation set-up is described in detail as well as the failure analysis procedure. A comparison between the experimental and numerical results is performed to provide confidence in the damage initiation predictability.

5.1 Experimental Set-up

The goal of the experiments was to identify the ultimate failure force of a tape-spring that is initially bent according to a specific radius of curvature. Two different tape-spring were produced and tested. The selected lay-up consists in a single UD ply between two plain woven plies for the first tape-spring, and between two twill woven plies for the second one. The geometrical and stacking sequence details are given in Appendix II. The two extremities of a bent tape-spring were attached into adapted jaws that are linked to a classical testing machine. The loading was applied through a cylindrical pin that is also linked to the testing machine as shown in Figure 34. The distance d between the two undeformed tape-spring arms was set equal to the pin diameter.

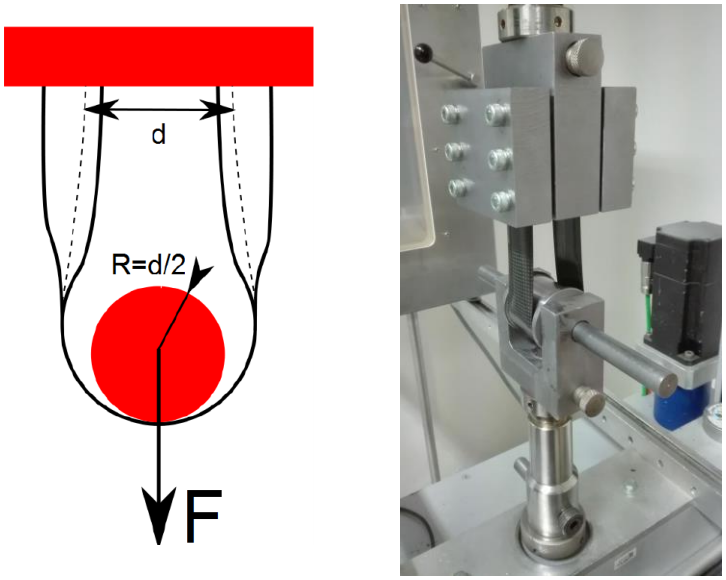

Figure 34. Testing tool principle (left) and testing device (right)

The tests were performed at the contractor's laboratory by using three different pin radius: R1, R2, and R3. The following testing sequence was followed for each sample:

- 1st run: load N applied with R1 pin,
- 2nd run: load N applied with R2 pin,
- 3rd run: load until failure applied with R3 pin.

It is very important to note that failure initiation was not taken into account and the same tape-spring sample was used for every test. However, cracking sounds were reported since the very beginning of the test, which indicates the presence of some kind of damage. The FE methodology presented in the following Section 5.2 does not consider damage propagation, thus only the first test can be considered for comparison purposes.

5.2 Tape-spring modeling

Tape-springs are thin-walled self-deployable strips that experience very large displacements when subjected to bending loads. Specifically, they can undergo opposite and equal sense bending as shown in Figure 35, depending if the longitudinal and transverse curvatures are applied in the same sense or not [68].

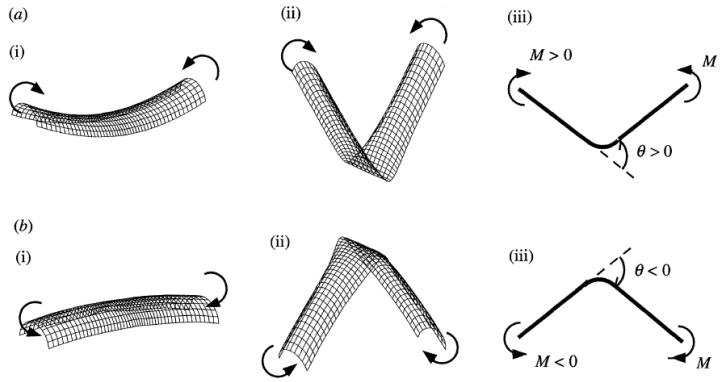

Figure 35. Opposite (top) and equal (bottom) sense bending of a tape spring [68]

As can be seen, the tape-spring folding is a highly geometric non-linear problem, which means that the solution needs to be found by splitting the simulation into small increments in order to find an approximate equilibrium configuration at each one. There are many possible solution methods to solve the problem, such as the Newton-Raphson, the Modified Newton-Raphson or the Arc Length method. A detailed description of these methods and others is given by Bathe [69]. The arc length method is a powerful numerical technique to solve global buckling problems. However, the tape-spring folding presents local buckling in-stabilities that cannot be handled by the arc length method. Therefore, the Newton-Raphson with artificial damping has demonstrated to be the best choice to achieve a converged solution [70].

It is important to note that the stabilization parameter should be as low as possible to ensure that the solution is not dominated by damping effects. This is particularly important for ultra-thin shell models due to their low bending stiffness. An optimal constant damping value could be found by comparing the strain energy against the energy dissipated due to viscous forces until the ratio between them is sufficiently small and a converged solution is obtained. However, this would require several trial-and-error analysis since the optimal value may change from different tape-spring configurations. Consequently, this approach was discarded in favor of an adaptive automatic stabilization

scheme, in which the ratio of the total stabilization energy to the total strain energy has been directly limited to 0.05 [71].

5.2.1 Simulation Set-up

The software Abaqus/Standard was chosen to perform the FE simulations. The first challenge encountered was to define a modelling strategy that could be used for any tape-spring and cylinder dimensions. A certain curvature is created in the middle of the tape-spring when a bending load is applied. This means that the tape-spring could be folded while the cylinder is subsequently placed in between by ensuring initial contact, which is required when treating contact problems within the finite element method. However, this approach would only be valid if the radius of curvature of the pin is smaller than the one of the tape-spring. Otherwise, the pin would not fit. The radius of curvature depends on several factors such as material properties or tape-spring initial geometry, thus it was necessary to define a strategy in which both the tape-spring and the pin are involved since the beginning of the simulation. The initial configuration of the finite element model is shown in Figure 36.

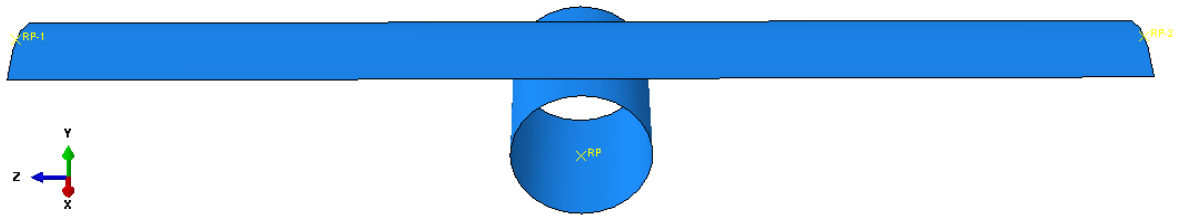

Figure 36. Finite element model of tape-spring and cylindrical pin

The cylindrical pin is modelled as a rigid body since it is assumed to be undeformable. It is associated with a reference point in its center that governs the motion of the entire cylinder. Regarding the tape-spring, two reference points RP1 and RP2 were created at the middle of the extremes in order to control the bending simulation. The nodes at the curved edges were connected to each reference point by using a multi point constraint. The tape-spring and the pin are placed together as illustrated in the Figure 36 by using the surface-to-surface contact definition without allowing separation. The goal is to fold the tape-spring while the cylinder follows the same displacement to eventually end up at the correct position.

The tape-spring has to be slightly pinched before starting to bend it. Otherwise, the initial fold might not occur at the middle point and the resulting local instabilities can cause the pin to separate from the tape-spring, among other convergence problems. This process is simulated by moving the pin in the positive y-direction as shown in Figure 37. The rigid pin is not allowed to move or rotate in the other directions to maintain symmetry. All degrees of freedom at the reference points RP1 and RP2 are also restrained in order to define the total displacement and the angle rotation in the next step.

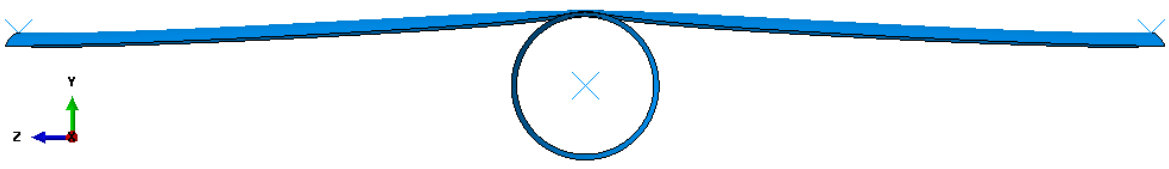

Figure 37. Pinching of the tape-spring

For the folding simulation, the rigid pin is allowed to move along the y-direction while the other degrees of freedom are kept retrained. The boundary conditions for the reference points RP1 and RP2 are defined as follows: a rotation about the x-axis is incremented from 0 rad to π/2. A displacement along the z-direction is defined such that the final distance between the two tape-spring arms is equal to the pin diameter. All other degrees of freedom are held zero. By doing the above, the test set-up configuration can be achieved in a single step. Initial contact between parts is ensured since the beginning of the simulation and convergence problems are avoided.

Finally, the pin is moved in the positive y-direction to simulate the tensile test. All degrees of freedom at the reference points RP1 and RP2 are restrained in order to simulate clamping conditions. The time interval must be chosen small enough so that the force is applied gradually through the rigid pin.

5.2.2 Failure Analysis Procedure

The failure analysis was carried out separately for the woven and the UD layers. The latter can be analysed by applying common failure theories, such as Tsai-Wu or maximum stress, to the stress components obtained from the finite element analysis. However, the woven layers require special considerations due to the stress gradient effects observed at the micromechanical level. The failure criterion proposed by Mallikarachchi and Pellegrino [45] has been presented in Section 2.4 as the most appropriate existing theory for woven composites. The criteria is expressed in terms of force and moment resultants. Therefore, the inputs required from the FE simulation are not the macro stresses as usual, but the section forces (SF) and moments (SM). For a section of thickness h, they are defined as follows [71]:

$$(SF1, SF2, SF3) = \int_{-h/2}^{h/2} (\sigma_{11}, \sigma_{22}, \sigma_{12}) dz \tag{76}$$

$$(SM1, SM2, SM3) = \int_{-h/2}^{h/2} (\sigma_{11}, \sigma_{22}, \sigma_{33}) z\, dz \tag{77}$$

It can be noted that the units are force and moment per unit width, thus they could be directly related to the macrostrains by means of the constitutive ABD matrix. According to the Abaqus documentation [71], the section force and moment resultants can only be given for the entire laminate. However, the strength parameters have been calculated in Section 4.3 from single-layer analyses, which means that the force and moment resultants must be evaluated at the layer level in order to apply the failure criterion. For this, Karkkainen et al. [72] proposed to calculate the multilayer mid-plane deformations as follows:

$$\begin{Bmatrix} [\varepsilon_0] \\ [\kappa] \end{Bmatrix} = \begin{bmatrix} [A] & [B] \\ [B] & [D] \end{bmatrix}_{ML}^{-1} \begin{Bmatrix} [N] \\ [M] \end{Bmatrix} \tag{78}$$

where [N] and [M] are the overall section force and moment resultants obtained from the FE simulation, and $[ABD]_{ML}$ is the stiffness matrix for the multilayer composite calculated in Section 4.2.3.

Now, the obtained mid-plane multilayer strain state must be adjusted to represent the actual strain in the single layer of interest. The strains are proportional to the curvature and may be assumed to vary linearly through the thickness of the laminate as follows:

$$\varepsilon_{ij} = \varepsilon_{ij}^{0} \pm h\kappa_{ij} \tag{79}$$

Finally, the force and moment resultant at the layer level can be calculated by using the modified strain given by Equation (79) together with the single-layer constitutive $[ABD]_{SL}$ matrices calculated in Section 4.2.1. The adjusted force and moment resultants will have to be calculated for each woven layer and then directly input to the failure criterion. The procedure above has to be repeated for each element of the tape-spring and every step of the simulation.

5.3 Numerical Results and Experimental Comparison

The tape-spring material properties were defined in Abaqus by creating a composite lay-up using the results obtained from each single-layer unit cell homogenization. Before discussing failure initiation, the force-extension results for both simulation and experiment are compared in Figure 38 below. Note that the plain/UD/plain configuration was analysed with (blue dashed line) and without (green dashed line) considering the stiffness reduction of the UD layer due to ply waviness.

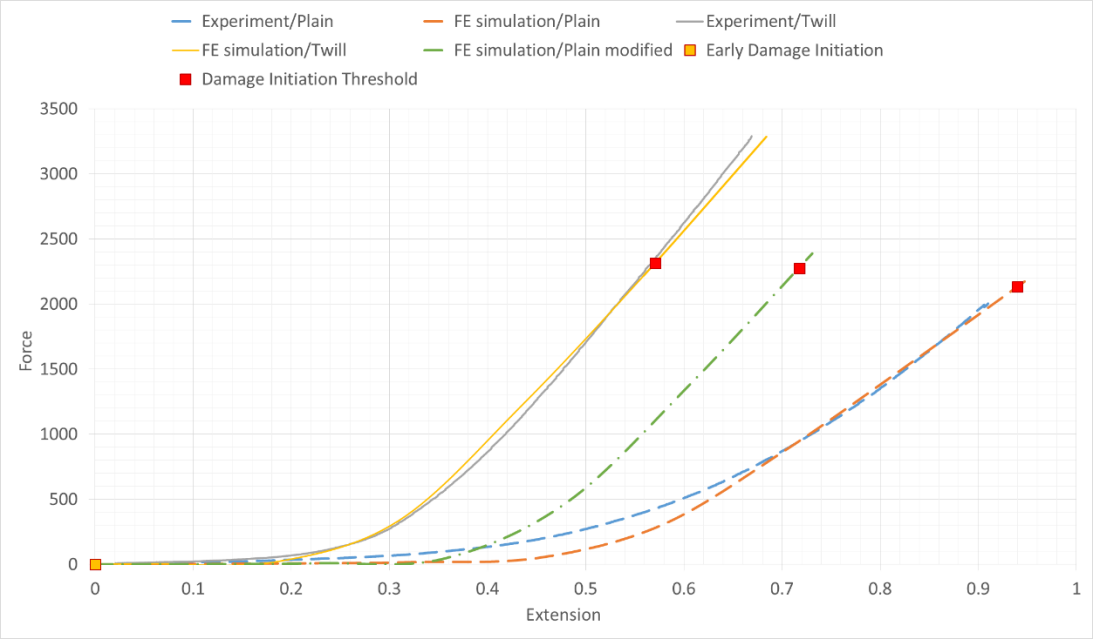

Figure 38. Force-extension tape-spring results

It can be observed that the finite element model captures reasonably well the global stiffness behavior for both plain and twill woven configurations. There is a first phase in which the displacement is very large for the load applied. The tape-spring conforms to the cylinder radius during this stage as shown in Figure 39 below. The difference between each tape-spring configuration is due to the different material properties and thickness, which affect the initial radius of curvature. It can be seen that the FE simulation does not perfectly capture the conforming phase of the plain woven configuration, where the experimental behavior is slightly stiffer. The FE model assumes only the in-plane stiffness reduction of the UD layer due to ply waviness. However, it does not take into account the

increase in bending stiffness caused by the undulation of the fibres in the out-of-plane direction. The influence of the UD ply waviness has been studied in Section 4.2.2 by assuming plane stress conditions, which does not allow to estimate through-the-thickness properties. The above explains why the first stage is not as well predicted as in the twill woven configuration, where UD play waviness is not present. In the second phase, the tape-spring is stretched and the in-plane stiffness plays a dominant role, so the prediction improves considerably.

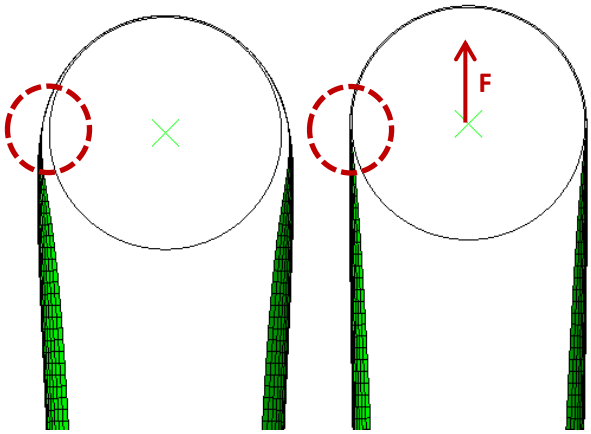

Figure 39. Stretching of a tape-spring

It can be concluded that the stiffness behaviour of the tape-springs is dominated by the UD layer. The type of woven layer does not make any important difference as long as the UD layer is kept flat. These findings were not obvious by just looking at the test results. It has been necessary to perform micrographs to observe a manufacturing defect that was unknown. This highlights the importance of controlling the manufacturing process of the tape-springs, as the ply waviness of the UD layer might be strongly affected by the layer shift between the woven layers.

Once the stiffness behaviour of the tape-springs have been analysed, the results of the failure analysis can be discussed. Failure was checked by evaluating the Equations (24), (25) and (26), which define the three projections of the failure criterion proposed by Mallikarachchi and Pellegrino [45]. The following failure indices were defined:

- FI-1, for failure under pure in-plane loading,
- FI-2, for failure under biaxial bending,
- FI-3, for failure due to the interaction between in-plane and bending loads.

The failure criteria was applied by using the uniaxial failure strengths listed in Table 18. First of all, the analysis was carried out by using the most conservative values obtained from the unit cell failure analysis, which indicate the initiation of the first microcracks. It was found that early failure initiation at the woven layers was already present in the folded configuration, with no tensile load applied through the pin. The contours of each failure index are shown in Figure 41. The results indicate that the initiation of failure is mainly sensitive to shear loading at the woven layers, which are oriented in the 45° direction. A sample graph showing the typical response of a ±45° woven laminate is shown in Figure 40 to better understand the damage mode under shear loading.

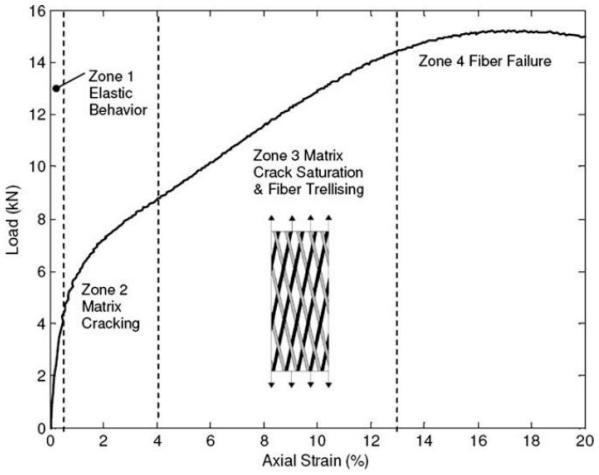

Figure 40. Typical shear response of woven composite [73]

It can be seen from Figure 40 above that the strain causing fiber failure is more than 10 times larger than the strain causing the first microcracks. This behaviour was also observed in the shear response for the two-ply weave composite shown in Figure 26. Therefore, the failure analysis indicates that matrix cracking begins to occur due to the axial strains at the folded region. This finding perfectly agrees with the crack sounds detected in the first folding cycles of the tape-springs.

A second failure analysis was carried out by using the less conservative uniaxial failure strengths listed in Table 18, which were estimated to avoid fiber breakage but assuming transverse and shear damage in the yarns. It was found that the load causing failure was very similar for both plain and twill woven configurations, as shown in Figure 38. The top woven layer was the first one failing in both cases. The contours of the three failure indices are shown in the following Figure 41.

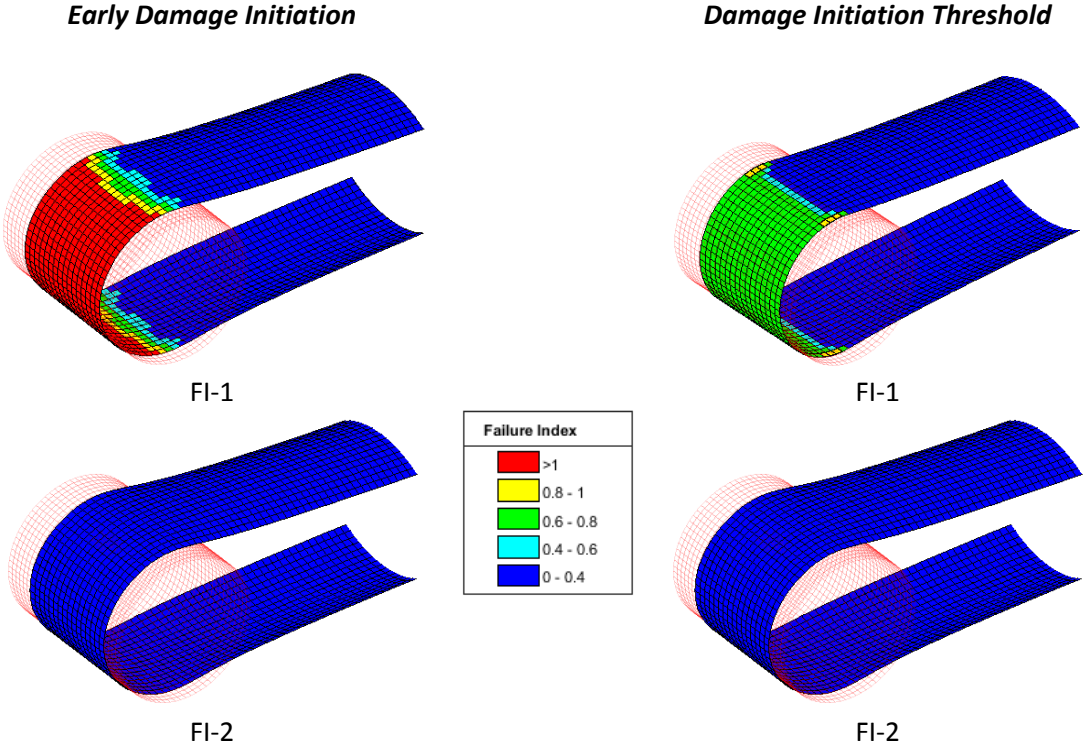

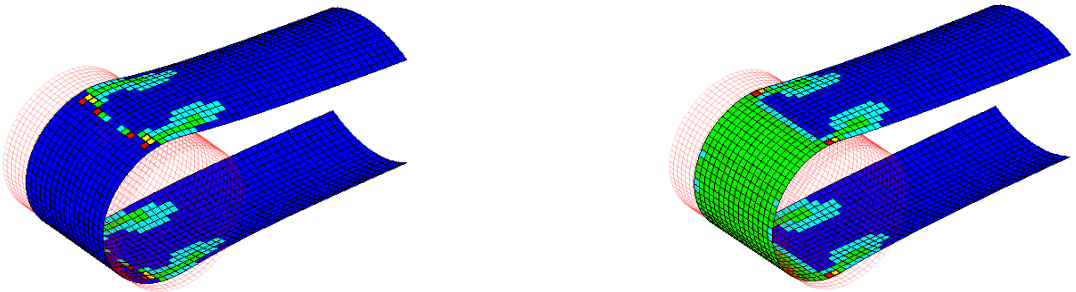

Figure 41. Failure indices for early damage initiation (left) and damage initiation threshold (right)

The damage initiation threshold was found at the transition zone due to the interaction between in-plane and out-of-plane loads. Some interesting observations can be made by comparing the results above with the images shown in Figure 42, which were taken during the experimental test at 2000 and ultimate failure. First, matrix crack saturation can be observed in the tape-spring at the 2000 load, which shows a slight change in color around the folded area. However, the experimental curves shown in Figure 38 do not present any drop in stiffness, but this does not mean there is no material damage. The overall stiffness is dominated by the UD layer, so small changes in the woven layers will barely affect the overall behavior. The second observation is related to the location of ultimate failure. The FE model predicts that fibers eventually begin to fail at the transition zone, which agrees with the experimental observations.

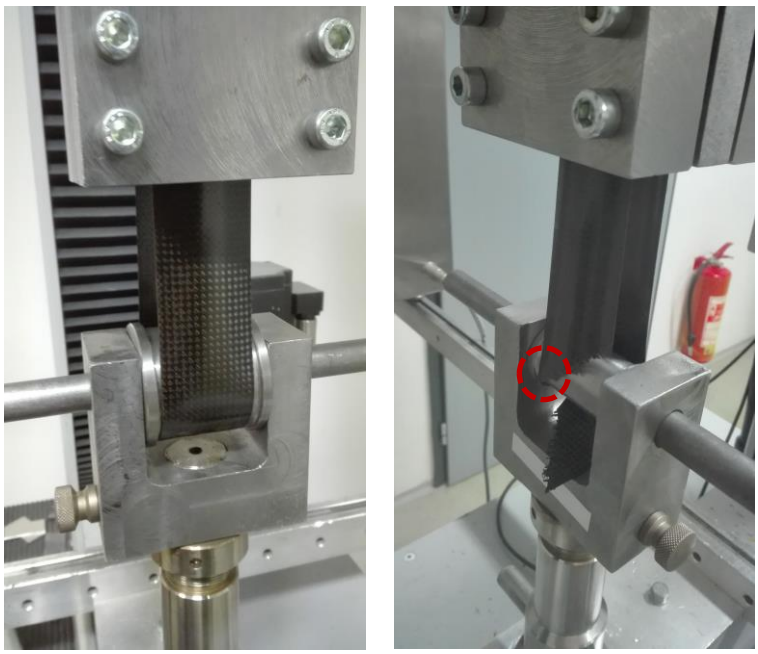

Figure 42. Tape-spring test at load X (left) and ultimate failure (right)

It can be concluded that the failure criteria presented by Mallikarachchi and Pellegrino [45] can predict the initial failure of woven composites under multi-axial loading conditions if the appropriate failure strength parameters are used. Mallikarachchi and Pellegrino showed that the criterion can predict ultimate failure of woven composites by using the strength values obtained from failure experiments. However, it has been seen that early damage mechanisms prior to ultimate failure, such

as matrix cracking, would not be captured by using these values. The effect of early damage initiation should be considered and further studied. Although it does not cause catastrophic failure, the presence of microcracks will affect the fatigue behaviour of the tape-springs, but the unique characteristics intrinsic to textile geometry and multi-axial loading conditions make a possible numerical analysis extremely challenging. Additional experimental tests will be required in the future.

5.4 Conclusions

The modelling techniques to study the response of tape-springs under multiaxial loading conditions have been defined in this chapter. The tape-springs present a highly nonlinear mechanical behaviour, thus the FE simulation has been setup to minimize local instabilities and avoid contact convergence issues. The material properties of the tape-spring have been defined by using the results obtained from the micro- and meso-scale analysis. It has been found that the type of weave pattern would not have appreciable effects on the stiffness behaviour of the tape-spring if there was no ply waviness of the UD layer. This means that the experimental results presented here should not be used to draw conclusions on which type of laminate configuration is better.

Initiation of failure has been studied by using a dedicated failure criteria based on the force and moment resultants. This criterion has been implemented in a Matlab based routine by using the strength parameters calculated from the unit cell analyses. The force and moment resultants obtained from the FE simulation are evaluated at the woven layer and failure is checked for each element of the tape-spring and every step of the simulation. Results have shown that early failure initiation occurs when the tape-springs are fully folded. This finding was expected since crack sounds can be detected when the tape-springs are folded for the first time. However, the extent and origin of the damage could not be estimated from the crack sounds. The failure analysis has shown that the tape-spring samples can be safely folded in equal sense without causing fibre breakage, but that intra-yarn matrix cracking could hardly be avoided due to the large strains in the folded region.

Chapter 6 Conclusions and Future work

6.1 Conclusions

Deployable structures using tape-springs have shown to be a promising option to minimize the volume occupied by satellites at launch and reduce launching costs. In the literature study, the requirements for satellite structures have been studied along with the mechanical behaviour of tape-springs. This review has provided insight into the most critical loading conditions as well as the advantages of using woven composites. The usually applied conventional micromechanical models for textile composites cannot be used to analyse the bending behaviour of tape-springs. Multi-axial loading requires techniques designed to capture stress gradients across the RVE. Therefore, the tape-springs studied in this thesis have been modelled on the basis of these premises.

The micromechanical models presented in this dissertation are based on an accurate description of the textile geometry. It has been shown how simple macro deformations can produce a very complex micro-stress field in the mesoscale. Thus special care has been taken in the definition and discretization of the RVE geometry. Woven composites present local variations in yarn cross-sections caused by the interlacing of warp and weft yarns. This effect has been taken into account in order to avoid issues of local interpenetrations, and thus construct a realistic unit cell model. Three different weave laminates have been chosen from the literature to validate the repeating unit cell approach and the application of periodic boundary conditions. It has been demonstrated that is acceptable to simplify the RVE definition by assuming homogenized material properties of the yarns. The stiffness of both plain and twill woven composites have been well-predicted when compared to experimental data.

The failure initiation analysis conducted for the validation of the methodology have shown that the first microcracks appear at very low applied strains as a consequence of the textile geometry and the stress gradients across the yarns. This type of failure is not easy to detect by experimental mechanical tests since the micro-cracks do not immediately propagate and the overall stiffness is not affected. However, acoustic energy measurements from the literature have demonstrated that early damage actually exists at the strain values predicted with the unit cell approach. For tensile and bending loading, it has been demonstrated that is acceptable to assume that the failure of the yarns is similar to that of a UD composite with the same constituent materials. However, this assumption is not valid when shear or twisting loads are present, as the critical shear strength depends on the location in the yarn. It has been proven that the shear strength of the fabric composite should be used as the critical shear strength value for the yarns in order to capture the failure initiation under these loading conditions.

Once the unit cell approach was validated, the laminates of a couple of tape-spring samples were analysed. The tape-springs were produced by using two woven layers with a ply of unidirectional

prepreg between them. Micrograph images were taken in order to measure the geometric parameters of the impregnated fibre bundles. The micrographs showed that it might exist significant undulation of the UD layer, thus an analytical method was used to estimate its influence on the in-plane stiffness properties. The results revealed that this manufacturing defect cannot be neglected since the overall stiffness behaviour is dominated by the unidirectional layer. It was concluded that the reason for the ply waviness might be due to the relative positioning between the woven layers. The UD ply tends to conform to the adjacent woven layer surfaces if the woven layers are not in-phase. Finally, the stiffness and the strength properties were homogenized by using the unit cell approach in order to analyse the tape-spring behaviour at the macroscopic level.

The Abaqus/Standard element solver was used to simulate the highly non-linear mechanical behavior of tape-springs subjected to multi-axial loading conditions. The tape-springs were initially bent according to a specific radius of curvature and tension was subsequently applied through a cylindrical pin. The loading state at the transition zone of the tape-spring is extremely complex due to the additional transverse moment induced by the flattening of the original transverse curvature. It was definitely not acceptable to assume a homogenous micro-stress field across the RVE, so a failure criterion based on force and moment resultants have been used to study failure initiation. The elastic behaviour of the tape-spring was proved to be practically independent on the weaving pattern of the woven layers. It can be stated that the important differences observed in the experimental tests are due to the ply waviness of the UD layer, but not to the type of woven layer itself. Early damage initiation was predicted at the woven layers when the tape-springs are fully bent due to the large strains induced at the folded region. No significant differences were observed between the plain and twill woven configurations, which is consistent with the finding that failure initiation is remarkably similar for different textile patterns when expressed in terms of applied strain. It can be concluded that intra-yarn matrix cracking will have to be accepted if the tape-springs presented here want to be used on future deployable space structures.

6.2 Recommendations for future work

There are several aspects of the multi-scale approach presented in this dissertation that could be further investigated. First, in terms of unit cell modelling, the properties of the impregnated yarns could be assigned locally instead of assuming them as homogenized continua. Local variations in the yarn cross sections have been taken into account to create the textile geometry, but not for the estimation of local variations in the fibre volume fraction. This might not affect the homogenized elastic properties, but its influence on damage could be a question for future consideration.

The failure analysis of the unit cell could be extended to incorporate damage propagation. However, the challenges are many. Existing formulae for the material degradation have several deficiencies, such as the arbitrary choice of empirical constants. Current research on meso-FE modelling of damage is still focused on simple in-plane loading conditions, thus incorporating a model of progressive failure for complex loading is a broad subject for further investigations.

The influence of UD ply waviness on the overall in-plane stiffness of hybrid laminates has been studied using an analytical model based on the fundamental assumptions of the Classical Laminate Theory, which does not allow to estimate the influence on the through-the-thickness properties. The FE-

homogenization approach could be used to estimate the material properties in every direction, but a realistic model of the undulated geometry would have to be generated first.

Incorporation of damage propagation at the meso-scale will not be easily related to the macro-scale. The simulation of both scales should be run in parallel in order to update the material and loading state. As an example, damage caused by bending loads will reduce the laminate thickness due to the stretching of the yarns, which will significantly affect the bending stiffness properties. Also, the straightening of the undulated UD layer could be possible due to matrix damage. The author believes that modeling damage propagation at both scales under multi-axial loading conditions is still unfeasible with the current computational capacity and numerical techniques. Further experimental tests are therefore recommended to study the effect of intra-yarn matrix cracking on the fatigue behavior of the tape-springs. The use of acoustic energy measurements is strongly recommended, since it might be possible to distinguish damage events such as fibre breakage.

References

[1] P. Warren, *Foldable member,* USA Patent 6,374,565 B1, 2002.

[2] Pellissetti, M. F., et al., "Static and Dynamic Reliability Analysis of Integral Satellite in View of Low Failure Probability," European Space Agency, (Special Publication) ESA SP, pp. 601., 2005.

[3] O. Soykasap, "Micromechanical models for bending behavior of woven composites," *Journal of spacecraft and rockets,* vol. 43, no. 5, pp. 1093-1100, 2006.

[4] R. R. Johnson, M. H. Kural and G. B. Mackey, "Thermal Expansion Properties of Composite Materials," *LOCKHEED MISSILES AND SPACE CO INC SUNNYVALE CA.,* 1981.

[5] Nassar, L. A., et al., "Spacecraft structures and launch vehicles," *Virginia Tech Report,* 2004.

[6] K. Iqbal and S. Pellegrino, "Bi-stable composite shells," *41st Structures, Structural Dynamics, and Materials Conference and Exhibit (p. 1385),* 2000.

[7] Y. Prigent, "A Finite Element Model of Bi-Stable Woven Composite Tape-Springs," KTH Royal Institute of Technology, Sweden, 2011.

[8] E. Picault, S. Bourgeois, B. Cochelin and F. Guinot, "On the folding and deployment of tape springs: A large displacements and large rotations rod model with highly flexible thin-walled cross-sections," *53rd AIAA/ASME/ASCE/AHS/ASC Structures, Structural Dynamics and Materials Conference 20th AIAA/ASME/AHS Adaptive Structures Conference 14th AIAA (p. 1956),* 2012.

[9] S. D. Guest and S. Pellegrino, "Analytical models for bistable cylindrical shells," *Proceedings of the Royal Society of London A: Mathematical, Physical and Engineering Sciences,* vol. 462, no. 2067, pp. 839-854, 2006.

[10] T. C. Henry, J. C. Riddick, R. P. Emerson and C. E. Bakis, "Characterization of the Effect of Fiber Undulation on Strength and Stiffness of Composite Laminates," *ARMY RESEARCH LAB ABERDEEN PROVING GROUND MD VEHICLE TECHNOLOGY DIRECTORATE,* 2015.

[11] B. Yang, V. Kozey, S. Adanur and S. Kumar, "Bending, compression, and shear behavior of woven glass fiber–epoxy composites," *Composites Part B: Engineering, 31(8),* pp. 715-721, 2000.

[12] B. N. Cox and G. Flanagan, "Handbook of analytical methods for textile composites," 1997.

[13] HexPly, "Prepreg Technology," 2013.

[14] A. Adumitroaie and E. J. Barbero, "Stiffness and strength prediction for plain weave textile reinforced composites," *Mechanics of Advanced Materials and Structures, 19(1-3),* pp. 169-183,

2012.

[15] S. Adanur, "Handbook of weaving," *CRC press,* 2000.

[16] G. Ernst, M. Vogler, C. Hühne and R. Rolfes, "Multiscale progressive failure analysis of textile composites," *Composites Science and Technology, 70(1),* pp. 61-72, 2010.

[17] C. C. Chamis, "Simplified composite micromechanics equations for hygral, thermal and mechanical properties," 1983.

[18] R. Younes, A. Hallal, F. H. Chehade and F. Fardoun, "Comparative review study on elastic properties modeling for unidirectional composite materials," *INTECH Open Access Publisher,* 2012.

[19] J. C. Halpin and J. L. Kardos, "The Halpin-Tsai equations: a review," *Polymer Engineering & Science, 16(5),* pp. 344-352, 1976.

[20] S. C. Quek, A. Waas, K. W. Shahwan and V. Agaram, "Compressive response and failure of braided textile composites: Part 2—computations," *International Journal of Non-Linear Mechanics,* vol. 39, no. 4, pp. 649-663, 2004.

[21] R. M. Christensen and F. M. Waals, "Effective stiffness of randomly oriented fibre composites," *Journal of Composite Materials,* vol. 6, no. 3, pp. 518-535, 1972.

[22] S. C. Tan, "Stress concentrations in laminated composites," *CRC Press,* 1994.

[23] T. Ishikawa and T. W. Chou, "Elastic behavior of woven hybrid composites," *Journal of Composite Materials,* vol. 16, no. 1, pp. 2-19, 1982.

[24] T. Ishikawa and T. W. Chou, "One-dimensional micromechanical analysis of woven fabric composites," *AIAA journal,* vol. 21, no. 12, pp. 1714-1721, 1983.

[25] N. K. Naik and V. K. Ganesh, "Prediction of on-axes elastic properties of plain weave fabric composites," *Composites Science and Technology,* vol. 45, no. 2, pp. 135-152, 1992.

[26] D. Scida, Z. Aboura, M. L. Benzeggagh and E. Bocherens, "A micromechanics model for 3D elasticity and failure of woven-fibre composite materials," *Composites Science and Technology,* vol. 59, no. 4, pp. 505-517, 1999.

[27] A. G. Prodromou, S. V. Lomov and I. Verpoest, "The method of cells and the mechanical properties of textile composites," *Composite structures,* vol. 93, no. 4, pp. 1290-1299, 2011.

[28] A. J., "Meso-mechanical analysis of composites by the method of cells," *Applied Mechanics Reviews,* vol. 42, p. 193–221, 1989.

[29] B. N. Cox, W. C. Carter and N. A. Fleck, "A binary model of textile composites—I. Formulation.,"

Acta metallurgica et materialia, vol. 42, no. 10, pp. 3463-3479, 1994.

[30] I. Verpoest and S. V. Lomov, "Virtual textile composites software WiseTex: Integration with micro-mechanical, permeability and structural analysis.," *Composites Science and Technology,* vol. 65, no. 15, pp. 2563-2574, 2005.

[31] A. Dixit, H. S. Mali and R. K. Misra, "Unit cell model of woven fabric textile composite for multiscale analysis," *Procedia Engineering,* vol. 68, pp. 352-358, 2013.

[32] M. Y. Matveev, "Effect of variabilities on mechanical properties of textile composites," PhD thesis, University of Nottingham, United Kingdom, 2015.

[33] N. V. De Carvalho, S. T. Pinho and P. Robinson, "Numerical modelling of woven composites: Biaxial loading.," *Composites Part A: Applied Science and Manufacturing,* vol. 43, no. 8, pp. 1326-1337, 2012.

[34] J. Xu, S. V. Lomov, I. Verpoest, S. Daggumati, W. V. Paepegem, J. Degrieck and M. Olave, "A progressive damage model of textile composites on meso-scale using finite element method: static damage analysis.," *Journal of Composite Materials,* vol. 48, no. 25, pp. 3091-3109, 2014.

[35] H. M. Y. C. Mallikarachchi and S. Pellegrino, "Quasi-static folding and deployment of ultrathin composite tape-spring hinges," *Journal of Spacecraft and Rockets,* vol. 48, no. 1, pp. 187-198, 2011.

[36] X. Tang and J. D. Whitcomb, "General techniques for exploiting periodicity and symmetries in micromechanics analysis of textile composites," *Journal of Composite Materials,* vol. 37, no. 13, pp. 1167-1189, 2003.

[37] J. Choi and K. K. Tamma, "Woven fabric composites—part I: Predictions of homogenized elastic properties and micromechanical damage analysis.," *International Journal for Numerical Methods in Engineering,* vol. 50, no. 10, pp. 2285-2298, 2001.

[38] W. Ruijter, J. Crookston, A. Long and A. Jones, "Computational meso-scale analysis of textile composites using adaptive finite element analysis," 47th AIAA/ASME/ASCE/AHS/ASC Structures, Structural Dynamics, and Materials Conference 14th AIAA/ASME/AHS Adaptive Structures Conference 7th (p. 2193), 2006.

[39] Q. Pan, S. Li and E. Sitnikova, "Multi-scale modelling and characterization of 3D woven composites using unit cells," 16th European Conference on Composite Materials, ECCM, 2014.

[40] R. L. Karkkainen and B. V. Sankar, "A direct micromechanics method for analysis of failure initiation of plain weave textile composites," *Composites Science and Technology,* vol. 66, no. 1, pp. 137-150, 2006.

[41] S. W. Tsai and E. M. Wu, "A general theory of strength for anisotropic materials," *Journal of composite materials,* vol. 5, no. 1, pp. 58-80, 1971.

[42] C. Kassapoglou, "Design and analysis of composite structures: with applications to aerospace structures," *John Wiley & Sons,* 2013.

[43] S. J. DeTeresa and G. J. Larsen, "Derived Interaction Parameters for the Tsai-Wu Tensor Polynomial Theory of Strength for Composite Materials," *ASME APPLIED MECHANICS DIVISION-PUBLICATIONS-AMD,* vol. 248, pp. 61-68, 2001.

[44] R. L. Karkkainen, B. V. Sankar and J. T. Tzeng, "A direct micromechanical approach toward the development of quadratic stress gradient failure criteria for textile composites," *Journal of Composite Materials,* vol. 41, no. 16, pp. 1917-1937, 2007.

[45] H. M. Y. C. Mallikarachchi and S. Pellegrino, "Failure criterion for two-ply plain-weave CFRP laminates," *Journal of Composite Materials,* vol. 47, no. 11, pp. 1357-1375, 2013.

[46] J. Yee., "Thin CFRP Composite Deployable Structures," PhD thesis, Department of Engineering, University of Cambridge, 2006.

[47] L. P. Brown and M. Sherburn, "TexGen V3.9.0," 2017.

[48] A. Doitrand, C. Fagiano, F. X. Irisarri and M. Hirsekorn, "Comparison between voxel and consistent meso-scale models of woven composites," *Composites Part A: Applied Science and Manufacturing,* vol. 73, pp. 143-154, 2015.

[49] G. Fang, B. El Said, D. Ivanov and S. R. Hallett, "Smoothing artificial stress concentrations in voxel-based models of textile composites," *Composites Part A: Applied Science and Manufacturing,* vol. 80, pp. 270-284, 2016.

[50] M. Ito and T. Chou, "An analytical and experimental study of strength and failure behavior of plain weave composites," *J Compos Mater,* vol. 32, no. 1, pp. 2-30, 1998.

[51] A. Long and L. Brown, “Modelling the geometry of textile reinforcements for composites: TexGen.,” *Composite Reinforcements for Optimum Performance,* pp. 239-264, 2011.

[52] H. Si and K. Gartner, “Meshing piecewise linear complexes by constrained Delaunay tetrahedralizations,” *Proceedings of the 14th International Meshing Roundtable,* pp. 147-163, 2005.

[53] S. Li and A. Wongsto, "Unit cells for micromechanical analyses of particle-reinforced composites," *Mechanics of materials,* vol. 36, no. 7, pp. 543-572, 2004.

[54] S. Lomov, D. Ivanov, I. Verpoest, M. Zako, T. Kurashiki, H. Nakai and S. Hirosawa, “Meso-FE modelling of textile composites: Road map, data flow and algorithms,” *Composites Science and Technology,* vol. 67, no. 9, pp. 1870-1891, 2007.

[55] W. Ruijter, "Analysis of mechanical properties of woven textile composite as functions of textile geometry," PhD thesis. University of Nottingham., 2008.

[56] D. S. Ivanov, "Damage analysis of textile composites," PhD Thesis, Katholieke Universiteit Leuven, 2009.

[57] S. V. Lomov and I. Verpoest, "Damage thresholds in tension of textile composites," KU Leuven, Belgium, 2012.

[58] S. Lomov, D. Ivanov, T. Truong, I. Verpoest, F. Baudry, K. Vanden Bosche and H. Xie, "Experimental methodology of study of damage initiation and development in textile composites in uniaxial tensile test," *Composites Science and Technology,* vol. 68, p. 2340–2349, 2008.

[59] M. Johnson and P. Gudmundson, "Broad-band transient recording and characterization of acoustic emission events in composite laminates," *Composites Science and Technology,* vol. 60, pp. 2803-2818, 2000.

[60] H. M. Y. C. Mallikarachchi, "Thin-Walled Composite Deployable Booms with Tape-Spring Hinges," PhD Thesis. University of Cambridge., 2011.

[61] V. Koissin, D. Ivanov, S. Lomov and I. Verpoest, "Fibre distribution inside yarns of textile composite: geometrical and FE modelling," Proceedings of the 8th International Conference on Textile Composites, 2006.

[62] L. Moreau-Gentien, "A study on the mechanical behaviour of woven fabric composites for the design of deployable space structures based on tape springs," École polytechnique fédérale de Lausanne, Switzerland, 2016.

[63] S. V. Lomov, A. E. Bogdanovich, D. S. Ivanov, K. Hamada, T. Kurashiki and M. Zako, "Finite element modelling of progressive damage in non-crimp 3D orthogonal weave and plain weave E-Glass composites," 2nd World conference on 3D fabrics, Greenville, South Carolina, USA, 2009.

[64] T. Lisle, C. Bouvet, M. Pastor, T. Rouault and P. Margueres, "Damage of woven composite under tensile and shear stress using infrared thermography and micrographic cuts," *Journal of materials science,* vol. 50, no. 18, pp. 6154-6170, 2015.

[65] M. H. Aliabadi, "Woven Composites," Imperial College Press, London, 2015.

[66] T. A. Bogetti, J. W. Gillespie and M. A. Lamontia, "Influence of ply waviness on the stiffness and strength reduction on composite laminates," *Journal of Thermoplastic Composite Materials,* vol. 5, no. 4, pp. 344-369, 1992.

[67] T. Ishikawa and T. W. Chou, "In-Plane Thermal Expansion and Thermal Bending Coefficients of Fabric Composites," *Journal of Composite Materials,* vol. 17, pp. 92-104, 1983.

[68] K. A. Seffen and S. Pellegrino, "Deployment Dynamics of Tape Springs," *Proceedings: Mathematical, Physical and Engineering Sciences,* vol. 455, no. 1983, pp. 1003-1048, 1999.

[69] K. J. Bathe, “Finite Element Procedures,” Prentice Hall, Pearson Education, Inc., 2006.

[70] O. Soykasa, “Analysis of tape spring hinges,” *International Journal of Mechanical Sciences,* vol. 49, p. 853–860, 2007.

[71] Abaqus, “Abaqus 6.14 documentation,” SIMULIA, United States of America, 2014.

[72] R. L. Karkkainen, B. V. Sankar and J. T. Tzeng, "Strength prediction of multi-layer plain weave textile composites using the direct micromechanics method," *Composites Part B: Engineering,* vol. 38, no. 7, pp. 924-932, 2007.

[73] D. R. Hufner and M. L. Accorsi, "A progressive failure theory for woven polymer-based composites," *Composite Structures,* vol. 89, no. 2, pp. 177-185, 2009.

[74] W. Wu, J. Owino, A. Al-Ostaz and L. Cai, "Applying Periodic Boundary Conditions in Finite Element Analysis," in *SIMULIA Community Conference*, Providence, United States, 2014.